LaTeX File (.tex, .sty, .cls, .bst, .bib)
Click here to download LaTeX File (.tex, .sty, .cls, .bst, .bib): Inoue_Back_GMS_2015_0322.tex
Generated using version 3.2 of the official AMS LaTeX template

Gross Moist Stability Assessment during TOGA COARE: Various Interpretations of Gross Moist Stability

Kuniaki Inoue, * Larissa E. Back

University of Wisconsin-Madison, Madison, Wisconsin

* *Corresponding author address:* Kuniaki Inoue, Department of Atmospheric & Oceanic Sciences, University of Wisconsin-Madison, 1225 W. Dayton St., Madison, WI 53706.

E-mail: inoue2@wisc.edu

ABSTRACT

Daily averaged TOGA COARE data are analyzed to investigate the mechanisms of convective amplification and decay. The gross moist stability (GMS) which represents moist static energy (MSE) export efficiency by the convection and large-scale circulations is studied, together with two quantities, called the critical GMS and the drying efficiency, which the authors coin. Our analyses reveal that convection is amplified/dissipated via negative/positive drying efficiency (i.e., sub-critical/super-critical GMS).

The authors illustrate that variability of the drying efficiency during the convective amplification phase is predominantly regulated by the vertical MSE advection (or vertical GMS) which imports MSE via a bottom-heavy vertical velocity profile (which is associated with negative vertical GMS) and eventually starts exporting MSE via a top-heavy profile (which is associated with positive vertical GMS). The variability of the drying efficiency during the decaying phase is, in contrast, controlled by the horizontal MSE advection (thus by the horizontal GMS), which efficiently exports MSE. The critical GMS, efficiency of moistening due to the diabatic forcing, is broadly constant throughout the convective life-cycle, indicating that the diabatic forcing always destabilizes the convective system in a constant manner.

The authors propose various ways of computing constant ”characteristic GMS”, and demonstrate that all of them are equivalent and can be interpreted as i) the critical GMS, ii) the GMS at the maximum precipitation, and iii) the combination of feedbacks between the radiation, the evaporation, and the convection. If the GMS is less/greater than that characteristic GMS, the convection is amplified/dissipated.

1. Introduction

Despite decades of advancement of conceptual theories and computational ability, it has been still challenging to correctly simulate tropical convective disturbances such as convectively coupled equatorial waves and the Madden-Julian oscillation (MJO) with realistic intensity and phase speed (e.g., Lin et al. 2006; Kim et al. 2009; Straub et al. 2010; Benedict et al. 2013). We know that one of the reasons for the difficulties is our lack of fundamental understanding of the interactions between deep convection and large-scale circulations in the tropics. However, to answer the question, "how, then, can we obtain better understanding of these interactions?", is a formidable task because the problems to solve are generally too intricate to separate each causality. To simplify the complex details in convective interactions, a conceptual quantity called the gross moist stability (GMS) has been investigated, and has proven useful in previous work. In this work, we utilize the GMS to look at mechanisms for convective amplification and decay in TOGA COARE data.

The GMS, which represents efficiency of moist static energy export by convection and associated large-scale circulations, was originated by Neelin and Held (1987) with a simple two-layer atmospheric model. They described it as "a convenient way of summarizing our ignorance of the details of the convective and large scale transients." Raymond et al. (2007) furthered this idea by defining the relevant quantity called the normalized gross moist stability (NGMS). Although different authors have used slightly different definitions of the NGMS (see a review paper by Raymond et al. (2009)), all the NGMS represent efficiency of export of some intensive quantity conserved in moist adiabatic processes per unit intensity of the convection. In this study, we utilize one version of the NGMS defined as

$$\Gamma \equiv \frac{\nabla \cdot \langle h\vec{v} \rangle}{\nabla \cdot \langle s\vec{v} \rangle} \tag{1}$$

where s is dry static energy (DSE), h is moist static energy (MSE), $\vec{v}$ is horizontal wind, the del-operator represents isobaric gradient, and the angle brackets represent a mass-weighted vertical integral from the tropopause to the surface pressure. In this study, we simply call Γ

the GMS instead of NGMS. We will show that this quantity and related ideas can be used to diagnose mechanisms for convective amplification and decay.

Previous GMS studies can be broadly categorized into two approaches: theoretical and diagnostic approaches. Although these two approaches are looking at the same quantity, namely the GMS, it is usually difficult to compare results from these two approaches to seek agreement between them. One of the difficulties arises from the simplification of vertical structures in the theoretical GMS studies.

Most of the theoretical GMS studies are inevitably dependent on an assumption of simple vertical structures. Historically, the GMS has been proven to be a powerful tool in the original quasi-equilibrium tropical circulation model framework (QTCM; Neelin and Zeng 2000). In the original QTCM framework, the temperature stratification is assumed to be close to a moist adiabat in hydrostatic balance, which forces the perturbation vertical velocity profiles to take a first baroclinic mode (e.g., Emanuel et al. 1994; Neelin and Zeng 2000). With the first baroclinic vertical velocity profile, the GMS is nearly constant, and provided that the main features of convectively coupled equatorial waves (CCEWs) are explained by the first baroclinic mode, the values of the GMS set the phase speed of the CCEWs (e.g., Emanuel et al. 1994; Neelin and Yu 1994; Tian and Ramanathan 2003; Raymond et al. 2009).

The recent observational studies, however, show that the vertical structures of the CCEWs are not explained only by the first baroclinic mode, but they requires the second baroclinic mode (e.g., Kiladis et al. 2009, and the references therein). Some theoretical studies have attempted to include the second baroclinic mode, and succeeded in producing realistic structures of the CCEWs (e.g., Mapes 2000; Khouider and Majda 2006; Kuang 2008a,b). In such realistic model frameworks, however, the GMS is not an attractive quantity because the second baroclinic mode inevitably causes singularities of the GMS, making it blow up to infinity at some points (e.g., Inoue and Back 2015).

Then, does this mean that the constant GMS is a purely theoretical quantity and cannot be compared with the real world? Surprisingly, and also perplexingly, Frierson et al. (2010)

found in the general circulation model experiments that the first baroclinic mode theory with constant GMS is adequate to explain the phase speed of the equatorial Kelvin waves. The reason why this works has not been articulated in the literature.

The recent diagnostic GMS studies have focused more on the time-dependent behavior of the GMS (e.g., Frierson 2007; Frierson et al. 2010; Hannah and Maloney 2011; Benedict et al. 2014; Hannah and Maloney 2014; Masunaga and L'Ecuyer 2014; Sobel et al. 2014; Inoue and Back 2015). Specifically, those studies have focused more on the aspect of the GMS as a quantity which describes the destabilization/stabilization mechanisms of the convective disturbances. Episodes of organized convective disturbances generally begin with a bottom-heavy vertical velocity profile which progressively evolves into a top-heavy profile as the convection develops. As in Fig. 1, a bottom-heavy profile with MSE-rich-lower-tropospheric convergence and MSE-poor-mid-tropospheric divergence leads to net import of MSE by the vertical circulation, and thus destabilizes the convective system via column moistening; this condition is associated with negative GMS. Conversely, a top-heavy profile with MSE-poor-mid-tropospheric convergence and MSE-rich-upper-tropospheric divergence is associated with net export of MSE and positive GMS, which causes the convection to decay. These destabilization/stabilization mechanisms play crucial roles in the dynamics of the CCEWs in cloud resolving model simulations (e.g., Peters and Bretherton 2006; Kuang 2008a).

There are two main objectives in this study. The first one is to demonstrate that the destabalization/stabilization mechanisms discussed above are crucial in the tropical convective dynamics in observational data, and that those mechanisms can be extracted by investigating the GMS. The second objective is to establish a "bridge" between the theoretical and diagnostic GMS studies, reducing the gaps between them by proposing a few hypotheses of how we can compare the theoretical constant GMS with more realistic time-dependent GMS.

The rest of this paper is structured as follows. Section 2 describes the data set we used (the TOGA COARE data set). Section 3 sets forth the theoretical framework of the relationship between the GMS and amplification/decay of convection. In this section, we introduce new quantities called the critical GMS and drying efficiency. By investigating those quantities in the TOGA COARE data, we demonstrate the amplification/decay mechanisms of the convection in section 4. In section 5, we extend our argument toward a more theoretical aspect, providing some hypotheses which potentially explain why the first baroclinic theory is adequate to explain the phase speed of the equatorial waves as claimed by Frierson et al. (2010). In this section, we also discuss some novel interpretations of the GMS. In section 6, we summarize our arguments.

2. Data description

We investigate the field campaign data from the Tropical Ocean Global Atmosphere Coupled Ocean-Atmosphere Response Experiment (TOGA COARE; Webster and Lukas 1992) to clarify the relationship between the GMS, vertical atmospheric structures (especially vertical velocity profiles), and convective amplification and decay. The TOGA COARE observational network was located in the western Pacific warm pool region. In this study, we analyze the data averaged over the spatial domain called the Intensive Flux Array (IFA), which is centered at 2° S, 156° E, bounded by the polygon defined by the meteorological stations at Kapingamarangi and Kavieng and ships located near 2° S, 158° E and 4° S, 155° E. The sounding data was collected during the 4-month Intensive Observing Period (IOP; 1 November 1992 to 28 February 1993) with 6 hourly time resolution. All variables are filtered with a 24-hour running mean for a reason explained in the next section.

The data set utilized was constructed by Minghua Zhang, who analyzed the sounding data by using an objective scheme called constrained variational analysis (Zhang and Lin 1997). In that scheme, the state variables of the atmosphere are adjusted by the smallest possible amount to conserve column-integrated mass, moisture, static energy, and momentum. See

Zhang and Lin (1997) for more detailed information about the scheme.

3. Theoretical framework

Following Yanai et al. (1973), we start with the vertically integrated energy and moisture equations

$$\frac{\partial \langle s \rangle}{\partial t} + \langle \vec{v} \cdot \nabla s \rangle + \langle \omega \frac{\partial s}{\partial p} \rangle = \langle Q_R \rangle + LP + SH \tag{2}$$

$$\frac{\partial \langle Lq \rangle}{\partial t} + \langle \vec{v} \cdot \nabla Lq \rangle + \langle \omega \frac{\partial Lq}{\partial p} \rangle = LE - LP \tag{3}$$

where $s \equiv C_p T + gz$ is dry static energy (DSE); $C_p T$ is enthalpy; gz is geopotential; Q_R is radiative heating rate; L is the latent heat of vaporization, P is precipitation rate; SH is surface sensible heat flux; q is specific humidity, E is surface evaporation; the angle brackets represent mass-weighted column-integration from 1000 hPa to 100 hPa; and the other terms have conventional meteorology meanings. Each quantity is averaged over the IFA. As in Raymond et al. (2009), assuming ω vanishes at the surface and tropopause pressures, utilizing the continuity equation, and taking integration by parts yields:

$$\frac{\partial \langle s \rangle}{\partial t} + \nabla \cdot \langle s \vec{v} \rangle = \langle Q_R \rangle + LP + SH \tag{4}$$

$$\frac{\partial \langle Lq \rangle}{\partial t} + \nabla \cdot \langle Lq \vec{v} \rangle = LE - LP. \tag{5}$$

In the deep tropics, temperature anomalies are small due to weak rotational constraints (Charney 1963, 1969; Bretherton and Smolarkiewicz 1989), and thus the DSE tendency and horizontal DSE advective terms in Eqs. 2 and 4 are often assumed to be negligible, which is called the weak temperature gradient approximation (WTG; Sobel and Bretherton 2000). When applying this assumption to observational data, however, we need to remove diurnal cycles of the temperature field, which is the primary exception to the negligible DSE tendency. Figures 2a and 2b illustrate the power spectra of the column DSE and column moisture tendencies. These figures show that most variance of the column DSE tendency is explained by the diurnal cycle, and the diurnal cycle of the column moisture tendency is, in contrast, much smaller than that of the column DSE tendency. Therefore, taking a daily running mean filter makes the column DSE tendency much less significant than the column moisture tendency as illustrated in Figs. 2c and 2d.

More attention is required when neglecting the DSE tendency because small temperature anomalies of the order of a Kelvin can have significant effects on vertical structures of convection (e.g., Kuang 2009, 2010), and Fig. 2c shows the DSE tendency is not perfectly zero. In this study, therefore, we interpret the WTG in a relatively relaxed way; that is, we assume the DSE anomalies to be negligible only when 1) filtered with time windows longer than 24 hours, and 2) vertically integrated and compared to the other terms in Eqs. 4 and 5 like a scale analysis. Small local temperature anomalies are not neglected when we examine vertical structures of the convection. This makes sense because our main purpose in using Eqs. 4 and 5 is to link the energy budgets to precipitation anomalies, and generally, precipitation anomalies are more correlated to the column moisture rather than the column DSE. Therefore, neglecting small column DSE anomalies doesn't hurt our conclusions. In those contexts, ignoring the column DSE tendency and adding Eqs. 4 and 5 yield

$$\frac{\partial \langle Lq \rangle}{\partial t} \simeq -\nabla \cdot \langle h\vec{v} \rangle + \langle Q_R \rangle + SF \tag{6}$$

where $h \equiv s + Lq$ is moist static energy (MSE) and $SF \equiv LE + SH$ is surface fluxes. Generally SH is negligible.

We now utilize a relationship between precipitation and column-integrated water vapor $\langle q \rangle$ (aka precipitable water or water vapor path), which was shown by Bretherton et al. (2004). They showed the relation in the form of

$$P = \exp[a(\langle q \rangle - b)] \tag{7}$$

where a and b are some constants calculated by nonlinear least squares fitting. Figure 3 illustrates the relationship between the precipitation and precipitable water during TOGA COARE. The patterns statistically agree with the proposed exponential relationship. This exponential relationship is, however, not so crucial for this study. The ideas described below are valid as long as the precipitation has positive correlation with the precipitable water, which can be observed in the figure. Equation 7 can be replaced by a linearized form

$$P = \frac{\langle q \rangle}{\tau_c} \tag{8}$$

where τ_c is a convective adjustment time scale as in the Betts-Miller parameterization (Betts 1986; Betts and Miller 1986), and the same conclusions can be drawn. Taking the natural logarithm of Eq. 7, and plugging it into Eq. 6 yields

$$\frac{L}{a}\frac{\partial \ln P}{\partial t} \simeq -\nabla \cdot \langle h\vec{v} \rangle + F \tag{9}$$

where $F \equiv \langle Q_R \rangle + SF$ is a diabatic source term.

Equation 9 indicates two convective phases:

$$\nabla \cdot \langle h\vec{v} \rangle - F < 0 \tag{10}$$

$$\nabla \cdot \langle h\vec{v} \rangle - F > 0. \tag{11}$$

According to Eq. 9, precipitation increases over time if a system is in the phase of Eq. 10 while it decreases in the phase of Eq. 11. Since the value of $\nabla \cdot \langle h\vec{v} \rangle - F$ is dependent of the intensity of the convection, it is advantageous to normalize it by the intensity of the convection so that we can take composites of all the convective events with different intensities in the TOGA COARE data, and from that context, the concept of the gross moist stability (GMS) appears. A similar normalization technique has been utilized by Hannah and Maloney (2011).

In this study, we define a case with positive $\nabla \cdot \langle s\vec{v} \rangle$ to be convectively active, and a case with negative $\nabla \cdot \langle s\vec{v} \rangle$ to be convectively inactive. Since we are interested in events when convection is happening, most of the analyses given below are conducted only for convectively active times. When convection is active, dividing Eqs. 10 and 11 by $\nabla \cdot \langle s\vec{v} \rangle$ yields

$$\Gamma - \Gamma_C < 0 \tag{12}$$

$$\Gamma - \Gamma_C > 0 \tag{13}$$

where

$$\Gamma_C = \frac{\langle Q_R \rangle + SF}{\nabla \cdot \langle s\vec{v} \rangle} \tag{14}$$

which we name critical GMS. Γ is gross moist stability (GMS) defined in Eq. 1, and we call the quantity $\Gamma - \Gamma_C$ the drying efficiency. This drying efficiency is an extension of a quantity called effective GMS (e.g., Bretherton and Sobel 2002; Peters and Bretherton 2005; Sobel and Maloney 2012), and is similar to a version of the effective GMS used in Hannah and Maloney (2014). We avoid calling it effective GMS because different authors use slightly different definitions, and because we include the horizontal MSE advection in the definition, which is different from the previous versions.

When $\Gamma - \Gamma_C$ is negative (Eq. 12), the system is in the amplifying phase in which convection is enhanced. Conversely, when $\Gamma - \Gamma_C$ is positive (Eq. 13), the system is in the decaying phase, leading to dissipation of the convection. (When convection is inactive with negative $\nabla \cdot \langle s\vec{v} \rangle$, those phases are reversed.) These hypotheses are not surprising because $\Gamma - \Gamma_C$ is equivalent to

$$-\frac{1}{\nabla \cdot \langle s\vec{v} \rangle} \frac{\partial \langle Lq \rangle}{\partial t} \sim -\frac{1}{P} \frac{\partial \langle q \rangle}{\partial t} \tag{15}$$

which represents efficiency of moisture discharge/recharge per unit intensity of convection, and the GMS and the critical GMS respectively represent contributions of MSE advection ($-\nabla \cdot \langle h\vec{v} \rangle$) and diabatic forcing ($F \equiv \langle Q_R \rangle + SF$) terms to that efficiency. Therefore, the phases of Eqs. 12 and 13 simply state that a moistened/dried system leads to amplification/dissipation of the convection. This simple concept is, nevertheless, useful from both diagnostic and theoretical perspectives.

In this study, we take composites of convective structures onto values of the drying efficiency. This composite method functions well because the drying efficiency is independent of the convective intensity (therefore is only a function of the convective structures), and is a good index of the convective stability[1]. Hence by using the drying efficiency composite method, we can demonstrate the connection between convective structures and the stability of moist convection.

4. Results and discussion

a. Drying efficiency and convective amplification/decay

First, we need to verify the hypotheses of the amplifying and decaying phases, Eqs. 12 and 13, for convectively active times during TOGA COARE. When computing Γ and Γ_C, as suggested by Raymond et al. (2009), the time filter was applied to the numerator and denominator before taking the ratio between them. All data points with $\nabla \cdot \langle s\vec{v} \rangle$ less than 10 Wm^{-2} were removed to exclude convectively inactive times and to avoid division by zero. Furthermore, since we apply a binning average method to $\Gamma - \Gamma_C$, we excluded 2.5% outliers from the left and right tails of the PDF of $\Gamma - \Gamma_C$ before taking composites in order to avoid biases due to very large and small values.

Figure 4a shows precipitation changes ($\delta P_i = P_{i+1} - P_{i-1}$) as a function of the drying efficiency $\Gamma - \Gamma_C$, averaged in 12.5-percentile bins. In the amplifying phase (negative $\Gamma - \Gamma_C$), the precipitation changes are positive, indicating the convection is enhanced; in the decaying phase (positive $\Gamma - \Gamma_C$), in contrast, the convection is attenuated. Figure 4b illustrates the probability of increase in precipitation as a function of the binned $\Gamma - \Gamma_C$. When $\Gamma - \Gamma_C$ is negative and large (-1.4 to -0.4) the probability of precipitation increase is greater than $\sim 70\%$ whereas when $\Gamma - \Gamma_C$ is positive and large (0.2 to 0.8) the precipitation decreases at $\sim 80\%$. As $\Gamma - \Gamma_C$ increases from -0.4 to 0.2, the probability of precipitation increase rapidly drops. Both Figs. 4a and 4b are consistent with the hypotheses of the amplification/decaying

[1]In this study, we use the word "stability" to refer to the effective gross moist stability (or drying efficiency), and not to conventional thermodynamic stability such as convective available potential energy (CAPE).

phases.

Figure 4c shows the precipitation as a function of the binned $\Gamma - \Gamma_C$. In the amplifying phase, the precipitation increases as $\Gamma - \Gamma_C$ becomes less negative, and reaches the maximum when $\Gamma - \Gamma_C$ is zero, or Γ is equal to Γ_C; in the decaying phase, the precipitation decreases with increase in $\Gamma - \Gamma_C$. This figure, together with Figs. 4a and 4b, indicates that values of the drying efficiency are statistically linked to convective development and dissipation; that is, convection generally begins with high efficiency of moistening (negative and large $\Gamma - \Gamma_C$), the drying efficiency gradually increases (i.e., $\Gamma - \Gamma_C$ becomes less negative) as the convection develops, and eventually starts to discharge moisture (positive $\Gamma - \Gamma_C$) leading to dissipation of the convection.

When interpreting Fig. 4 and the other drying efficiency figures, however, one caution is required; that is, those figures don't include any information about time. They were plotted in order of the drying efficiency from the most efficient to the least efficient, or in order of stability from the most unstable to the most stable. Therefore, they are not ordered in time, and the length of the x-axis does not represent the actual duration of the corresponding structure. Nevertheless, because every phenomenon statistically evolves from unstable to stable conditions, those figures represent statistical convective life-cycle; the convection generally evolves from negative and large $\Gamma - \Gamma_C$ to positive and large $\Gamma - \Gamma_C$.

b. Variability of drying efficiency

In the last subsection, we verified that when the drying efficiency $\Gamma - \Gamma_C$ is negative/positive, convection is enhanced/attenuated, respectively. Now let us investigate which processes cause variability of the drying efficiency, making the convection amplify or dissipate. In other words, we examine how moist convection evolves from unstable (negative $\Gamma - \Gamma_C$) into stable (positive $\Gamma - \Gamma_C$) conditions.

Variability of $\Gamma - \Gamma_C$ is separated into contributions of the GMS (or advective terms) and of the critical GMS (or diabatic forcing terms). Furthermore, GMS can be divided into horizontal and vertical components as

$$\Gamma = \Gamma_H + \Gamma_V \tag{16}$$

where

$$\Gamma_H = \frac{\langle \vec{v} \cdot \nabla h \rangle}{\nabla \cdot \langle s\vec{v} \rangle}$$
$$\Gamma_V = \frac{\langle \omega \frac{\partial h}{\partial p} \rangle}{\nabla \cdot \langle s\vec{v} \rangle}.$$

Therefore, variability of the drying efficiency can be explained by three components, changes in the horizontal GMS Γ_H, the vertical GMS Γ_V, and the critical GMS Γ_C. Figure 5 shows those three components as a function of the binned $\Gamma - \Gamma_C$. By comparing the amount of the slope of each component with the slope of $\Gamma - \Gamma_C$, we can determine which processes explain the variability of the drying efficiency when it evolves from negative to positive values.

In this figure, Γ_C is broadly constant and maintains positive values around $0.25 \sim 0.5$ along all the values of $\Gamma - \Gamma_C$. (Although it slightly varies, the variations are less significant compared to the other two terms.) This indicates that Γ_C always decreases the value of $\Gamma - \Gamma_C$ toward negative values, and thus forces the convective system toward the amplifying phase. The combination of radiative heating and surface fluxes, therefore, constantly destabilizes the convection as a moisture (or MSE) source, increasing efficiency of moistening (or decreasing the drying efficiency) during both the amplifying and decaying phases, and doesn't contribute to the variability of $\Gamma - \Gamma_C$. In other words, a transition of the convection from the amplifying into the decaying phase is not regulated by the radiative heating and surface fluxes. A more detailed statistical analysis of why Γ_C is broadly constant is explained in section 4d.

In the amplifying phase (i.e., $\Gamma - \Gamma_C < 0$), most of the slope of $\Gamma - \Gamma_C$ is explained by Γ_V. This indicates that vertical MSE advection predominantly regulates the convective evolution from the amplifying into the decaying phases. In this phase, Γ_H is broadly constant and nearly zero, implying the horizontal MSE (or moisture) advection doesn't contribute to amplification of the convection. When $\Gamma - \Gamma_C$ is ~ -1.4, the values of Γ_H, Γ_V, and Γ_C are ~ -0.2, ~ -0.7, and ~ 0.5, respectively. Hence the system is primarily moistened by the vertical MSE advection, radiative heating, and surface fluxes. As the convection evolves towards the decaying phase, Γ_V becomes less negative, which indicates moistening via vertical advection becomes less efficient. At $\Gamma - \Gamma_C \simeq -0.5$, Γ_H and Γ_V are nearly zero while Γ_C is ~ 0.5. In this stage, only the radiative heating and surface fluxes destabilize the convection. As the convection develops further to greater $\Gamma - \Gamma_C$, the vertical advection starts to discharge moisture (i.e., positive Γ_V), leading to dissipation of the convection. Therefore, what drives the convection from the amplifying into the decaying phase is the vertical GMS Γ_V, which at the beginning destabilizes the convection via moistening, followed by stabilization via discharge of moisture. During that evolution, Γ_C constantly destabilizes the system, resisting the stabilization by the vertical advection.

In the decaying phase (i.e., $\Gamma - \Gamma_C > 0$), in contrast, the slope of Γ_H nicely matches the slope of $\Gamma - \Gamma_C$. Therefore, the drying efficiency in the fastest dissipation stage is mainly controlled by the horizontal MSE advection. Γ_V also keeps positive values in this phase, indicating the vertical advection also exports MSE and dries the system. But the horizontal advection dries the system more efficiently (i.e., $\Gamma_H > \Gamma_V$). Γ_C is relatively constant with positive values, making $\Gamma - \Gamma_C$ smaller. Therefore, in the decaying phase, both horizontal and vertical advection stabilize the convection by providing drier conditions while the radiative heating and surface fluxes destabilize the convection by supplying MSE anomalies into the convective system.

c. Variability of vertical GMS

We have shown that in the amplifying phase, most of the variability of the drying efficiency is explained by the vertical GMS Γ_V. Now we investigate how Γ_V varies. During TOGA COARE, 94% of the total variance of $\langle \omega \partial h / \partial p \rangle$ is explained by the variance of ω. Thus, the variability of Γ_V is mainly due to the fluctuations of ω profiles. The relationship between Γ_V and ω has been pointed out by previous studies (e.g., Back and Bretherton 2006; Peters and Bretherton 2006; Raymond et al. 2009; Masunaga and L'Ecuyer 2014; Inoue and

Back 2015). Those studies have demonstrated that bottom-heavy ω profiles which import MSE via lower level convergence and middle level divergence are associated with negative (or close to negative) values of Γ_V while top-heavy profiles with middle level convergence and upper level divergence export MSE from the atmospheric column, causing positive and large Γ_V.

Figure 6a illustrates the relationship between Γ_V and ω profiles for convectively active times in the TOGA COARE data. The blue/red shaded contours represent ascent/descent motions. As described above, negative and large Γ_V is associated with bottom-heavy ω shapes, and as Γ_V increases ω becomes more top-heavy. When the convection is inactive ($\nabla \cdot \langle s\vec{v} \rangle$ is negative; in Fig. 6b), the relation is reversed; that is, negative and large Γ_V corresponds to top-heavy ω with lower tropospheric descending motion while positive and large Γ_V is associated with bottom-heavy profiles with upper tropospheric descending motion.

Figure 6b, together with Fig. 6a, completes a life-cycle of the convection. The convection is initialized with small and positive Γ_V during negative $\nabla \cdot \langle s\vec{v} \rangle$ (in Fig. 6b), and Γ_V increases as the convection develops. After passing the singularity of Γ_V (or zero $\nabla \cdot \langle s\vec{v} \rangle$), it becomes a negative and large value that corresponds to bottom-heavy motion (in Fig. 6a), which gradually deepens with increase in Γ_V and reaches the other singularity. Again, the sign of Γ_V flips, and it becomes negative and large when the convection is in a stratiform shape (in Fig. 6b), and as the stratiform convection is dissipated the value of Γ_V becomes less negative, completing the life-cycle. Since our main interest in this study is convective amplification/decay mechanism instead of initialization/termination processes, we concentrate on analyses of the data points with positive $\nabla \cdot \langle s\vec{v} \rangle$.

Interestingly, the anomalous temperature field exhibits coherent structures to ω profiles. Figure 7 shows anomalous temperature profiles with respect to the binned Γ_V, which is compared with Fig. 6a. When Γ_V is negative with bottom-heavy ω profiles, an anomalously warm layer can be observed around 600 hPa. The height of this stable layer matches the upper limit of the bottom-heavy ω. This temperature structure is commonly observed in convectively coupled equatorial waves (e.g., Straub and Kiladis 2003; Kiladis et al. 2009; Frierson et al. 2010). We speculate this inversion layer works like a lid which prevents the bottom-heavy ω profiles from becoming top-heavy. Previous TOGA COARE studies (e.g., Johnson et al. 1996, 1999) have posited that this layer is produced by melting processes of cloud droplets around 0°C. An important role of this layer in convective dynamics has been pointed out by, for instance, Kikuchi and Takayabu (2004), who claimed that moistening below this 0°C level may be an influential factor for development of the convection. We can rephrase this statement from a perspective of the GMS; that is, the 0°C stable layer prevents the bottom-heavy ω profiles from evolving into a top-heavy profile, which maintains the negativity of Γ_V, and destabilizes the convective system by enhancing the efficiency of moistening.

d. Constancy of critical GMS

Now that we have shown the critical GMS Γ_C stays relatively constant in both the amplifying and decaying phases (in Fig. 5), let us consider why that is the case. The argument given below is based on the linearity of the diabatic forcing terms (i.e., $F \equiv \langle Q_R \rangle + SF$) with respect to the DSE advection (i.e., $\nabla \cdot \langle s\vec{v} \rangle$). In theoretical GMS studies where a vertical structure is assumed to be a single mode, the GMS is time-independent (e.g., Neelin and Held 1987; Emanuel et al. 1994; Neelin and Yu 1994; Tian and Ramanathan 2003; Fuchs and Raymond 2007; Raymond et al. 2009; Sugiyama 2009; Sobel and Maloney 2012). That is equivalent to saying that the MSE advection can be linearly parameterized with intensity of the convection. However, Inoue and Back (2015) demonstrated that the time-independent GMS is not an accurate approximation especially on a couple day time-scales (although it is theoretically tractable). In this subsection, we will show that linear approximation of the diabatic forcing terms is, instead, more consistent with the observational data during TOGA COARE than that of the advective terms (compare Figs. 8c and 8f, which are scatter plots of F and $\nabla \cdot \langle h\vec{v} \rangle$ as a function of $\nabla \cdot \langle s\vec{v} \rangle$). This linear approximation of F provides us with a new interpretation of the GMS, which will thoroughly explained in this subsection and section 5.

Generally, the column radiative heating $\langle Q_R \rangle$ can be expressed as

$$\langle Q_R \rangle = r_R LP + Q_0 \tag{17}$$

where r_R is a cloud-radiative feedback constant and Q_0 is the clear-sky column raditive heating (e.g., Bretherton and Sobel 2002; Peters and Bretherton 2005). The DSE budget equation (Eq. 4) with the WTG is

$$\nabla \cdot \langle s\vec{v} \rangle \simeq \langle Q_R \rangle + LP. \tag{18}$$

Here we neglected the surface sensible heat flux. By rearranging Eq. 18 and plugging it into Eq. 17, we obtain

$$\langle Q_R \rangle = \gamma_R \nabla \cdot \langle s\vec{v} \rangle + \beta_R \tag{19}$$

where

$$\gamma_R \equiv \frac{r_R}{1 + r_R} \tag{20}$$

and

$$\beta_R \equiv \frac{Q_0}{1 + r_R}. \tag{21}$$

Figure 8a illustrates a scatter plot of $\langle Q_R \rangle$ versus $\nabla \cdot \langle s\vec{v} \rangle$ with the least square fitting. $\langle Q_R \rangle$ which has a high correlation with $\nabla \cdot \langle s\vec{v} \rangle$ (0.83) is well represented by the linear equation (Eq. 19).

Similarly, applying a positive correlation between surface fluxes and precipitation (e.g., Raymond et al. 2003; Back and Bretherton 2005; Araligidad and Maloney 2008; Riley Dellaripa and Maloney 2015), we obtain

$$SF = r_S LP + S_0 \tag{22}$$

where r_S represents an evaporation-moisture convergence feedback (e.g., Zebiak 1986; Back and Bretherton 2005), and S_0 is the surface fluxes at zero precipitation. In a similar way to

Eq. 19, utilizing the DSE budget equation with the WTG, Eq. 22 can be rearranged into

$$SF = \gamma_S \nabla \cdot \langle s\vec{v} \rangle + \beta_S \tag{23}$$

where

$$\gamma_S \equiv \frac{r_S}{1 + r_R} \tag{24}$$

and

$$\beta_S \equiv \frac{S_0 + r_R S_0 - r_S Q_0}{1 + r_R}. \tag{25}$$

Now we need to verify the validity of Eq. 23 in the observational data during TOGA COARE. Figure 8b is a scatter plot of SF versus $\nabla \cdot \langle s\vec{v} \rangle$ with the least square fit. The linear fit seems adequate enough to express the overall pattern of SF. As pointed out by previous studies, there is a positive correlation (0.57) between SF and intensity of the convection ($\nabla \cdot \langle s\vec{v} \rangle$ in this study). However, this positive correlation is not the only reason for the validity of the linear approximation of SF because the correlation between $\nabla \cdot \langle h\vec{v} \rangle$ and $\nabla \cdot \langle s\vec{v} \rangle$ is also high (0.55) and is comparable to that of SF. (The correlation of $\langle \omega \partial h / \partial p \rangle$ is even higer (0.63).) For the linear approximation of SF to be more accurate than that of $\nabla \cdot \langle h\vec{v} \rangle$, besides the positive correlation, small variance of SF compared to the other MSE budget terms (especially $\nabla \cdot \langle h\vec{v} \rangle$) is required. That can be seen in the values of the mean square errors of the linear fits given in Fig. 8. The mean square error for SF is about an order smaller than that for $\nabla \cdot \langle h\vec{v} \rangle$, which makes the linear approximation of SF more accurate compared with the linear approximation of $\nabla \cdot \langle h\vec{v} \rangle$. This smaller mean square error is simply due to the smaller variance of SF than that of $\nabla \cdot \langle h\vec{v} \rangle$.

Hence, for Eq. 23 to be valid, two conditions have to be satisfied: 1) SF is positively correlated with $\nabla \cdot \langle s\vec{v} \rangle$, and 2) variance of SF is much smaller than that of $\nabla \cdot \langle h\vec{v} \rangle$. The second condition is violated in longer time-scales such as the MJO scale, in which variance of SF is comparable to the other MSE budget terms (e.g., Maloney 2009; Benedict et al. 2014; Inoue and Back 2015). Furthermore, Riley Dellaripa and Maloney (2015) found that relationship between SF and precipitation significantly varies along a life-cycle of the MJO. It must be noted, therefore, that our arguments are only applicable to the convective dynamics in shorter time-scales (a couple day scales), which we are examining in this study by using daily averaged data. We will give more thorough discussion about the time-scale in section 4g.

Since both $\langle Q_R \rangle$ and SF are well represented by the least square fittings, it is the case for F, the combination of $\langle Q_R \rangle$ and SF. Adding Eqs. 19 and 23 yields

$$F \equiv \langle Q_R \rangle + SF = \gamma \nabla \cdot \langle s\vec{v} \rangle + \beta \tag{26}$$

where

$$\gamma \equiv \gamma_R + \gamma_S = \frac{r_R + r_S}{1 + r_R} \tag{27}$$

and

$$\beta \equiv \beta_R + \beta_S = \frac{Q_0 + S_0 + r_R S_0 - r_S Q_0}{1 + r_R} \tag{28}$$

which is shown in Fig. 8c with a high correlation coefficient (0.76).

Interestingly, Eq. 26 can be simplified further because, in the TOGA COARE data, the intercept of the $\langle Q_R \rangle$ fitting (β_R; in Fig. 8a) cancels out the intercept of the SF fitting (β_S; in Fig. 8b), causing the intercept of the F fitting (β; in Fig. 8c) to be negligible. Hence, Eq. 26 becomes

$$F \simeq \gamma \nabla \cdot \langle s\vec{v} \rangle. \tag{29}$$

Therefore, the critical GMS is

$$\Gamma_C \equiv \frac{F}{\nabla \cdot \langle s\vec{v} \rangle} \simeq \gamma. \tag{30}$$

The good fit describes why Γ_C stays relatively constant in both the amplifying and decaying phases in Fig. 5 in the TOGA COARE data set. (Of course, this linear approximation is not perfect, and thus Γ_C slightly varies in Fig. 5.) The amplifying and decaying phases, Eqs. 12 and 13, can be written as

$$\Gamma - \gamma < 0 \tag{31}$$

$$\Gamma - \gamma > 0. \tag{32}$$

The phases in these equations suggest that a convective system is amplified (dissipated) if the GMS is less (greater) than the feedback constant γ. Thus, how much convection can grow may be controlled by a value of γ.

We do not yet understand why the intercept is close to zero. It would be interesting to examine whether this disappearance of the intercept β is just a coincidence or is due to some physical constraints. Although we are not sure if this is the case in general, we can, at least, use the simple linearization (Eq. 29) for a simple model framework, which gives many insightful ideas discussed in section 5.

When dealing with anomalous MSE budgets instead of the total budgets, the argument becomes much simpler because we don't have to worry about the intercept β. We can take anomalies of the MSE budgets to obtain the similar relations to Eqs. 31 and 32 as follows:

$$\Gamma' - \gamma < 0 \tag{33}$$

$$\Gamma' - \gamma > 0 \tag{34}$$

where

$$\Gamma' \equiv \frac{\nabla \cdot \langle h\vec{v} \rangle'}{\nabla \cdot \langle s\vec{v} \rangle'} \tag{35}$$

is anomalous GMS. (Interpretations of the anomalous GMS are discussed in Inoue and Back (2015).) Equations 33 and 34 respectively correspond to the amplifying and decaying phases, and precipitation reaches the maximum when

$$\Gamma'|_{P_{max}} = \gamma. \tag{36}$$

In spite of the simplicity of the anomalous form, we include the mean state in our argument below in order to obtain further interesting ideas discussed in section 5.

e. Drying efficiency and convective structures

We have thus far shown the followings:

- Bottom-heaviness of ω is responsible for negative vertical GMS Γ_V, which is associated with import of moisture (or MSE) in the amplifying phase.

- That bottom-heaviness might be related to the middle tropospheric 0°C stable layer.

- In the amplifying phase, horizontal GMS Γ_H is close to zero, indicating small contribution of the horizontal advection to the moistening.

- Critical GMS Γ_C is broadly constant due to the linearity of $\langle Q_R \rangle$ and SF and due to the cancellation of the intercept β.

- In the decaying phase, both vertical and horizontal advection export column moisture (i.e., $\Gamma_H, \Gamma_V > 0$), but the horizontal advection exports more efficiently (i.e., $\Gamma_H > \Gamma_V$).

Those points are summarized in Figs. 9 and 10, which illustrate vertical structures of ω, anomalous temperature, vertical and horizontal MSE advection as a function of the binned $\Gamma - \Gamma_C$.

When $\Gamma - \Gamma_C$ is negative, ω is in a bottom-heavy shape (Fig. 9a) which imports MSE from the lower troposphere (Fig. 10a), whereas the horizontal advection plays only a little role in the moistening processes in this phase (Fig. 10b). The bottom-heaviness of ω might be related to the anomalously warm layer at about 600 hPa, observed in Fig. 9b. Since Γ_C is broadly constant, it doesn't change the vertical structures, but it contributes to the shift of the x-axis compared to Fig. 6a. For instance, in Fig. 6a, ω starts to become top-heavy at $\Gamma_V \simeq -0.25$, whereas in Fig. 9a it does at $\Gamma - \Gamma_C \simeq -0.45$. The difference between those values is due to Γ_C, which is roughly constant.

When $\Gamma - \Gamma_C$ is positive, ω with a top-heavy shape (Fig. 9a) exports MSE from the upper-troposphere (Fig. 10a). Besides that, horizontal advection also exports MSE from the lower-to-middle troposphere as depicted in Fig, 10b. This behavior of the horizontal advection is not surprising. Generally, at the very end of the dissipative stage of convection, the atmospheric column is anomalously moist compared to the surrounding environment.

Therefore, horizontal winds in any direction lead to drying of the atmospheric column, causing positive Γ_H as shown in Fig. 10b.

The mechanisms described above imply that tropical convection is a self-regulating system. Variability of moistening/drying efficiency is predominantly regulated by the shape of vertical velocity profiles (in the amplifying phase) and by the atmospheric column moisture (in the decaying phase), both of which are parts of the convective system. Moreover, timing of a transition from the amplifying into the decaying phase may be determined by the feedbacks between the radiation, the evaporation, and the convection. A convective episode, which starts with shallow convection, spontaneously enhances the convection via bottom-heavy ω. Deepened convection, in turn, starts to dry out the system via top-heavy ω, dissipating the convection. In the decaying phase, horizontal winds also dry the system by carrying dry air from the surrounding environment into the convective system or carrying moist air from the system to the environment. Therefore, we might be able to refer to the amplifying/decaying phases as "self-amplifying/self-decaying" phases.

f. Convective intensity and drying efficiency

Now we investigate a qualitative relation between convective intensity and vertical structures. Utilizing the MSE budget equation (Eq. 6) and the linearized precipitation equation (Eq. 8), we obtain

$$\tau_c \frac{\partial LP}{\partial t} = -\nabla \cdot \langle h\vec{v} \rangle + F. \tag{37}$$

Dividing both sides by $\nabla \cdot \langle s\vec{v} \rangle$ and applying Eqs. 17 and 18 yield

$$\frac{\partial \ln(LP + \beta_R)}{\partial t} = -\frac{r_R + 1}{\tau_c}(\Gamma - \Gamma_C) \tag{38}$$

where r_R and β_R are the constants defined in Eq. 19, and we neglected the sensible heat flux. This equation is only applicable to the data points with positive $\nabla \cdot \langle s\vec{v} \rangle$. We solve this equation for P, and obtain

$$LP = (LP_0 + \beta_R) \exp\left\{ \frac{r_R + 1}{\tau_c} \Lambda \right\} - \beta_R \tag{39}$$

where

$$\Lambda \equiv -\int_{t_0}^{t} (\Gamma - \Gamma_C)\, \mathrm{d}t$$

and P_0, t_0 are some reference precipitation and time. This equation demonstrates that the rate of precipitation increase is determined by Λ, a time-integration of the efficiency of moistening (negative drying efficiency). There are three ways to increase Λ: 1) decrease Γ via bottom-heavy ω, 2) increase Γ_C via enhanced feedbacks between the convection, the radiation, and the evaporation (according to Eqs. 27 and 30), and 3) increase the duration in which $\Gamma - \Gamma_C$ is negative. Therefore, those indicate that, bottom-heavy ω, strong radiative-cloud and evaporation-convergence feedbacks, long duration of shallower vertical motion profiles, can all intensify the consequential precipitation maximum. In Figs. 7 and 9b, we observed the 0°C stable layer in the middle troposphere that might keep the bottom-heaviness of ω. Hence, it would be interesting to test whether there is a positive correlation between the intensity of the 0°C inversion and the intensity of the consequential convection.

g. Target time-scale

When examining MSE budgets in tropical variability, it is always necessary to clarify which time-scale is the target because MSE budgets behave in significantly different ways among different time-scales (e.g., Inoue and Back 2015). In this study, we have taken composites with respect to the values of $\Gamma - \Gamma_C$, which is, according to Eq. 15, equivalent to negative column water vapor tendency per unit intensity of convection. Therefore, it is the most natural to think that our analyses herein represent the convective structures with the highest frequency in the data set. We have removed the diurnal cycle, thus the highest-frequency variability in the TOGA COARE data is disturbance with ~2 day periodicity (see Fig. 1 in Inoue and Back 2015). We examined the structures of the high-frequency disturbances using the same data (not shown), and found significant resemblances with the structures shown in Figs. 6, 7, 9, and 10.

By using a low-pass (or band-pass) filter, we can apply this method to lower-frequency variability such as Kelvin waves. In section 4d, however, we used an assumption that the variance of SF is much smaller than that of $\nabla \cdot \langle h\vec{v} \rangle$, and this assumption is violated as the time-scale gets longer. Figure 11 illustrates the ratio of the variance of $\nabla \cdot \langle h\vec{v} \rangle$ to the variance of SF as a function of cut-off period of the Lanczos low-pass filter with 151 weights. As the cut-off period increases, the periodicity of the time-series becomes longer. This figure shows that as the periodicity becomes longer, the varinace of $\nabla \cdot \langle h\vec{v} \rangle$, which dominates SF on short time-scales, becomes more comparable to the variance of SF. This indicates that our methodology herein is only applicable to short time-scales, such as mesoscale convective systems and fast propagating equatorial waves, and not applicable to the MJO scale.

5. More discussion

a. Various interpretations of GMS

As described above, the gross moist stability Γ is a highly time-dependent quantity which significantly varies from negative to positive along the convective life-cycle. Recent diagnostic studies have focused more on time-dependent characteristic of Γ (e.g., Frierson 2007; Frierson et al. 2010; Hannah and Maloney 2011; Benedict et al. 2014; Hannah and Maloney 2014; Masunaga and L'Ecuyer 2014; Sobel et al. 2014; Inoue and Back 2015); on the other hand, constant GMS has been popularly utilized in theoretical studies (e.g., Neelin and Held 1987; Emanuel et al. 1994; Neelin and Yu 1994; Tian and Ramanathan 2003; Fuchs and Raymond 2007; Raymond et al. 2009; Sugiyama 2009; Sobel and Maloney 2012). Inoue and Back (2015) claimed that the constant vertical GMS may be a good approximation for the MJO, but is not for short time-scale variability such as inertia-gravity waves or Kelvin waves. Nevertheless, an assumption of constant vertical GMS has been used for explaining phase speed of convectively coupled equatorial waves (e.g., Emanuel et al. 1994; Neelin and Yu 1994; Tian and Ramanathan 2003; Raymond et al. 2009). Then, some natural questions will come up; that is, "How can we interpret the constant GMS which is not observed in the real world, and how can we estimate a meaningful value of the constant GMS in observational data?" Fortunately, all the analyses we have shown so far in this paper have already provided the answers for these questions. We will clarify these answers through a couple steps.

First, we need to clarify how to estimate a single meaningful value of the GMS. There have been a couple different ways proposed from different contexts. We now show that all of them are almost equivalent in the TOGA COARE data set. Those different definitions are listed as follows:

i. GMS defined at the maximum anomalous precipitation (e.g., Sobel and Bretherton 2003), or

$$\Gamma'_{max} \equiv \Gamma'|_{P_{max}} \tag{40}$$

ii. GMS computed from a scatter plot of anomalous $\nabla \cdot \langle h\vec{v} \rangle$ versus $\nabla \cdot \langle s\vec{v} \rangle$ (e.g., Table 1 in Inoue and Back 2015), or

$$\tilde{\Gamma}' \equiv \frac{\overline{\nabla \cdot \langle h\vec{v} \rangle' * \nabla \cdot \langle s\vec{v} \rangle'}}{\overline{\nabla \cdot \langle s\vec{v} \rangle'^2}} \tag{41}$$

iii. GMS computed from a scatter plot of non-anomalous $\nabla \cdot \langle h\vec{v} \rangle$ versus $\nabla \cdot \langle s\vec{v} \rangle$ (e.g., Fig. 9 in Raymond and Fuchs 2009), or

$$\tilde{\Gamma} \equiv \frac{\overline{\nabla \cdot \langle h\vec{v} \rangle * \nabla \cdot \langle s\vec{v} \rangle}}{\overline{\nabla \cdot \langle s\vec{v} \rangle^2}} \tag{42}$$

iv. GMS in a quasi-steady state (e.g., Eq. 7 in Kuang 2010), or

$$\Gamma_0 \equiv \frac{\overline{\nabla \cdot \langle h\vec{v} \rangle}}{\overline{\nabla \cdot \langle s\vec{v} \rangle}} \tag{43}$$

There are a couple more different methods to estimate quasi-time-independent GMS (e.g., Yu et al. 1998; Chou et al. 2013), but all of them can be qualitatively categorized in one of the above lists. We include the horizontal advection in the definitions above although it is generally not included.

From Eq. 36, Γ'_{max} is equal to γ, which represents a combination of the radiative-convective and the evaporation-convergence feedbacks according to Eq. 27. Now γ can be statistically calculated by a least square method as

$$\gamma = \frac{\overline{F' * \nabla \cdot \langle s\vec{v} \rangle'}}{\overline{\nabla \cdot \langle s\vec{v} \rangle'^2}}. \tag{44}$$

But from the MSE budget equation, γ is also expressed as

$$\gamma = \frac{\overline{\{\partial \langle h \rangle / \partial t + \nabla \cdot \langle h\vec{v} \rangle'\} * \nabla \cdot \langle s\vec{v} \rangle'}}{\overline{\nabla \cdot \langle s\vec{v} \rangle'^2}} \tag{45}$$

Since $\partial \langle h \rangle / \partial t$ and $\nabla \cdot \langle s\vec{v} \rangle'$ (or P') are almost out of phase (e.g., Inoue and Back 2015), covariance between them becomes negligible if the time-series is long enough. Therefore, we obtain

$$\Gamma'_{max} = \gamma = \tilde{\Gamma}' \tag{46}$$

Moreover, in the TOGA COARE data, the intercept of the least square fit of F (β; in Fig. 8c) is negligible. This indicates that the least square fit of $\nabla \cdot \langle h\vec{v} \rangle$ as a function of $\nabla \cdot \langle s\vec{v} \rangle$ also has to go through the origin as shown in Fig. 8f where the least square fit is almost identical to the regression line through the origin. Therefore, we obtain

$$\tilde{\Gamma}' = \tilde{\Gamma} \tag{47}$$

and this equation can be rearranged into

$$\tilde{\Gamma}' = \Gamma_0 \tag{48}$$

Furthermore, Fig. 8d shows the horizontal component of $\tilde{\Gamma}'$, $\tilde{\Gamma}'_H$, is close to zero (0.035), hence

$$\tilde{\Gamma}' \simeq \tilde{\Gamma}'_V \tag{49}$$

where $\tilde{\Gamma}'_V$ is the vertical component of $\tilde{\Gamma}'$.

The above arguments demonstrate that all the time-independent GMSs defined in the different ways (i–iv) are equivalent, and are all equal to γ in the TOGA COARE data. We call them the characteristic GMS. From the definition of γ (Eq. 27), it represents a combination of the radiative-convective and the evaporation-convergence feedbacks, and moreover, it is equal to the critical GMS Γ_C from Eq. 30, which is the threshold between the amplifying and the decaying phases (Eqs. 12 and 13). Therefore, we can interpret all the characteristic GMSs, Γ'_{max}, $\tilde{\Gamma}'$, $\tilde{\Gamma}$, and Γ_0 as follows:

First: A critical value which determines the threshold between the amplifying and the decaying phases of the convection at a given place.

Second: A value of the time-dependent GMS at the precipitation maximum.

Third: A combination of the radiative-convective and the evaporation-convergence feedbacks.

These interpretations may explain a mechanism of tropical convection. At a given place, convection is enhanced if a value of the GMS is below the characteristic GMS at that place, and that sub-critical GMS is primarily due to bottom-heavy ω profiles (or a positive second baroclinic mode). Eventually, the ω profile becomes a top-heavy shape (or a negative second baroclinic mode), causing the GMS to be greater than the threshold, which leads to decay of the convection. This mechanism is consistent with Masunaga and L'Ecuyer (2014). Furthermore, the threshold may be determined by the feedback mechanisms between the radiation, the evaporation, and the convection, which is a novel view of the feedback mechanisms and convective dynamics.

b. More hypotheses of characteristic GMS

In this subsection, we will propose a few hypotheses related to the characteristic GMS which we inferred based on the analyses above and previous GMS studies. (In this subsection, we ignore the horizontal characteristic GMS which was negligible in the TOGA COARE data.) The first hypothesis is that the phase speed of observable equatorial waves is predominantly regulated by vertical diabatic heating profiles at the convective maximum, and therefore all of the characteristic GMSs (Eqs. 40∼43) adequately explain the phase speed of the waves because they are all equivalent to the GMS at the precipitation maximum. This hypothesis might imply that the characteristic GMS is the quantity which corresponds to the GMS in the quasi-equilibrium tropical circulation model (QTCM) framework with a first baroclinic mode (e.g., Emanuel et al. 1994; Neelin and Yu 1994). This hypothesis is consistent with Frierson et al. (2010), who found in the general circulation model experiments that the phase speed of equatorial Kelvin waves is well explained with the time-mean GMS and the first baroclinic mode theory by Tian and Ramanathan (2003). They also found that the time-mean GMS is close to the GMS at the convective maximum which they expect to be the most important for determining the phase speed, concluding the time-mean GMS values are adequate to explain the phase speed of the waves. Their claims are decidedly consistent with our analyses.

The first and second interpretations of the characteristic GMS discussed above imply that values of the characteristic GMS are related to the height of the maximum diabatic heating. A value of the (time-dependent) GMS increases in a convective life-cycle as the vertical velocity (or the diabatic heating) profile grows into a top-heavy shape (as in Fig. 6a), and when the GMS exceeds the characteristic GMS, the convection starts to dissipate. Hence the value of the characteristic GMS might determine how top-heavy a diabatic heating profile can become; the greater the characteristic GMS is, the top-heavier the profile can become before decaying. If the value of the characteristic GMS is small, the convection is unlikely to reach the upper-troposphere with strong intensity, and thus, as claimed by Frierson et al. (2010), the convection is less efficient at stabilizing the upper-troposphere via latent heat release, leading to less stable atmosphere in general and to slower wave speeds.

In such a manner, a single vertical structure at the convective maximum might be adequate to explain the phase speed of the waves. This view is reinforced by the recent theoretical work by Fuchs et al. (2012), who has claimed that more top-heavy diabatic heating profiles lead to faster propagating waves.

Furthermore, the third interpretation of the characteristic GMS leads us to the other novel hypothesis that the phase speed of the waves is regulated by the feedbacks between the radiation, the evaporation, and the convection; the stronger the feedbacks are, the faster the wave propagates with top-heavier diabatic heating profiles. This idea could be integrated into a simple model framework, which will be left for future work.

c. *Applications of characteristic GMS*

Finally, we will briefly talk about some applications of the time-independent characteristic GMS. As described above, the critical GMS Γ_C is roughly equal to the characteristic GMS. Therefore, we don't need any information about $\langle Q_R \rangle$ and SF for estimating Γ_C. Figure 12 demonstrates that idea. Here Γ_C was replaced by mean GMS Γ_0. This figure shows that the theory is statistically valid; when $\Gamma - \Gamma_0$ is negative/positive, the convection is enhanced/dissipated as shown in Fig. 4.

The same idea can be illustrated in a different way as in Fig. 13 where the red/blue dots represent data points in which the precipitation increases/decreases, and the slope of the black solid line represents the characteristic GMS. This figure shows that if a data point is located below the GMS line in this plane, the convection is enhanced (red dot), and if a point is located above the GMS line, the convection decays (blue dot). Therefore, we can statistically infer whether a given condition is in the amplifying phase or in the decaying phase only from the information of MSE and DSE advection. This figure also illustrates that convection tends to fluctuate around the GMS line in the $\nabla \cdot \langle h\vec{v} \rangle$-versus-$\nabla \cdot \langle s\vec{v} \rangle$ plane.

Moreover, in section 4f, we suggested that the more negative $\Gamma - \Gamma_C$ is, the more intense the consequential convection becomes. Hence, at a give value of $\nabla \cdot \langle s\vec{v} \rangle$, a data point located further below from the GMS line can potentially become stronger than a data point closer to the GMS line. This idea might be useful for validating numerical weather/climate models in the deep tropics, which is generally challenging.

6. Summary

We have investigated the convective amplification/decay mechanisms in short time-scale disturbances by examining the gross moist stability (GMS; Γ) and its relevant quantities in the TOGA COARE data set. We coined two quantities, namely the critical GMS (Γ_C) and the drying efficiency ($\Gamma - \Gamma_C$). $\Gamma - \Gamma_C$ is an extension of the effective GMS, which represents negative precipitable water tendency per unit intensity of convection. Γ and Γ_C respectively represent the contributions of the advective terms ($\nabla \cdot \langle h\vec{v} \rangle$) and the diabatic forcing terms ($F \equiv \langle Q_R \rangle + SF$) to the drying efficiency.

First, we verified that the convection is amplified/attenuated via negative/positive drying efficiency; Figures 4a and 4b show that the precipitation is enhanced/attenuated when $\Gamma - \Gamma_C$ is negative/positive. Therefore, we call the phases with negative/positive $\Gamma - \Gamma_C$ the amplifying/decaying phases. We also found that the precipitation reaches the maximum when $\Gamma - \Gamma_C$ is zero, or the GMS is equal to the critical GMS (Fig. 4c).

Next, we investigated which processes explain the variability of $\Gamma - \Gamma_C$. By doing so, we can clarify which processes destabilize the convection, and how the convection is forced to transition from the amplifying into the decaying phases. In the amplifying phase (i.e., $\Gamma - \Gamma_C < 0$), most of the variability of $\Gamma - \Gamma_C$ is explained by the vertical GMS Γ_V (Fig. 5), which indicates that the convective transition from the amplifying into the decaying phases is primarily regulated by the vertical MSE advection. Convection with a bottom-heavy ω profile efficiently imports MSE via low level convergence (negative Γ_V), which leads to further enhancement of the convection via column moistening. As the convection develops, the ω profile gradually becomes top-heavy, starting export of the column MSE from the upper troposphere (positive Γ_V), which leads to dissipation the convection, finishing the amplifying phase. During the amplifying phase, the horizontal GMS Γ_H broadly stays close to zero, indicating that the horizontal MSE advection doesn't contribute the column moistening in this phase. In the decaying phase ($\Gamma - \Gamma_C < 0$), in contrast, the variability of $\Gamma - \Gamma_C$ is mainly explained by Γ_H. In this phase, the vertical advection also exports MSE (i.e., $\Gamma_V > 0$), but the horizontal advection exports more efficiently (i.e., $\Gamma_H > \Gamma_V$), leading to decay of the convection via column drying.

Throughout the convective life-cycle, the critical GMS Γ_C broadly stays constant with a positive values (Fig. 5). This indicates that the column radiative heating and surface fluxes always destabilize the convective system by supplying the MSE sources in a constant manner. The constancy of Γ_C is due to the linearity of the diabatic forcing with respect to the intensity of the convection (which is the case only in short time-scale disturbances), and also due to the disappearance of the intercept β in Eq. 26. Although we are not sure whether or not the negligible β is the case in general, the linear approximation of the diabatic forcing provides us with a simple model framework in which we can interpret the GMS in novel ways.

In section 5, we have demonstrated that all of the following definitions of the constant GMSs are equivalent in the TOGA COARE data: i) anomalous GMS at the precipitation maximum (Γ'_{max}), ii) GMS computed from a scatter plot of anomalous $\nabla \cdot \langle h\vec{v} \rangle$ versus $\nabla \cdot \langle s\vec{v} \rangle$ ($\tilde{\Gamma}'$), iii) GMS computed from a scatter plot of non-anomalous $\nabla \cdot \langle h\vec{v} \rangle$ versus $\nabla \cdot \langle s\vec{v} \rangle$ ($\tilde{\Gamma}$), iv) steady state GMS (Γ_0); all of which are collectively called the characteristic GMS. The characteristic GMS can be interpreted as follows: I) a critical value which determines the threshold between the amplifying and the decaying phases, II) a value of the GMS at the precipitation maximum, and III) a combination of the radiative-convective and the evaporation-convergence feedbacks.

These interpretations provide us with some novel hypotheses about the convective amplification/decay mechanisms. That is, convection is amplified/dissipated if the GMS is less/greater than the characteristic GMS, which is determined by the feedbacks between the radiation, the evaporation, and the convection. Also, high-frequency convective disturbances can be seen as fluctuations around the slowly changing characteristic GMS in the plane of Fig. 13.

Furthermore, based on our analyses and previous studies, we have proposed some hypotheses. We first hypothesized that the characteristic GMS is adequate to explain the phase speed of the equatorial waves. If that is the case, it might suggest that the phase speed of the waves is regulated by the feedbacks between the radiation, the evaporation, and the convection. We also hypothetically speculated that the characteristic GMS is the quantity which corresponds to the GMS in the QTCM framework. Those hypotheses should be examined in future work.

Acknowledgments.

This research is supported by NASA Grant NNX12AL96G.

REFERENCES

Araligidad, N. M. and E. D. Maloney, 2008: Wind-driven latent heat flux and the intraseasonal oscillation. *Geophys. Res. Lett.*, **35**, L04 815, doi:10.1029/2007GL032746.

Back, L. E. and C. S. Bretherton, 2005: The relationship between wind speed and precipitation in the pacific ITCZ. *J. Climate*, **18**, 4317–4328, doi:10.1175/JCLI3519.1.

Back, L. E. and C. S. Bretherton, 2006: Geographic variability in the export of moist static energy and vertical motion profiles in the tropical Pacific. *Geophys. Res. Lett.*, **33**, L17 810, doi:10.1029/2006GL026672.

Benedict, J. J., E. D. Maloney, A. H. Sobel, D. M. Frierson, and L. J. Donner, 2013: Tropical intraseasonal variability in version 3 of the GFDL atmosphere model. *J. Climate*, **26**, 426–449, doi:10.1175/JCLI-D-12-00103.1.

Benedict, J. J., E. D. Maloney, A. H. Sobel, and D. M. W. Frierson, 2014: Gross moist stability and MJO simulation skill in three full-physics GCMs. *J. Atmos. Sci.*, **71**, 3327–3349, doi:10.1175/JAS-D-13-0240.1.

Betts, A. K., 1986: A new convective adjustment scheme. Part I: Observational and theoretical basis. *Q.J.R. Meteorol. Soc.*, **112**, 677–691, doi:10.1002/qj.49711247307.

Betts, A. K. and M. J. Miller, 1986: A new convective adjustment scheme. Part II: Single column tests using GATE wave, BOMEX, ATEX and arctic air-mass data sets. *Q.J.R. Meteorol. Soc.*, **112**, 693–709, doi:10.1002/qj.49711247308.

Bretherton, C. S., M. E. Peters, and L. E. Back, 2004: Relationships between water vapor path and precipitation over the tropical oceans. *J. Climate*, **17**, 1517–1528, doi:10.1175/1520-0442(2004)017⟨1517:RBWVPA⟩2.0.CO;2.

Bretherton, C. S. and P. K. Smolarkiewicz, 1989: Gravity waves, compensating subsidence and detrainment around cumulus clouds. *J. Atmos. Sci.*, **46**, 740–759, doi: 10.1175/1520-0469(1989)046⟨0740:GWCSAD⟩2.0.CO;2.

Bretherton, C. S. and A. H. Sobel, 2002: A Simple Model of a Convectively Coupled Walker Circulation Using the Weak Temperature Gradient Approximation. *J. Climate*, **15**, 2907–2920, doi:10.1175/1520-0442(2002)015⟨2907:ASMOAC⟩2.0.CO;2.

Charney, J. G., 1963: A note on large-scale motions in the tropics. *J. Atmos. Sci.*, **20**, 607–609, doi:10.1175/1520-0469(1963)020⟨0607:ANOLSM⟩2.0.CO;2.

Charney, J. G., 1969: A further note on large-scale motions in the tropics. *J. Atmos. Sci.*, **26**, 182–185, doi:10.1175/1520-0469(1969)026⟨0182:AFNOLS⟩2.0.CO;2.

Chou, C., T.-C. Wu, and P.-H. Tan, 2013: Changes in gross moist stability in the tropics under global warming. *Clim Dyn*, **41**, 2481–2496, doi:10.1007/s00382-013-1703-2.

Emanuel, K. A., J. D. Neelin, and C. S. Bretherton, 1994: On large-scale circulations in convecting atmospheres. *Q.J.R. Meteorol. Soc.*, **120**, 1111–1143, doi:10.1002/qj.49712051902.

Frierson, D. M. W., 2007: Convectively coupled Kelvin waves in an idealized moist general circulation model. *J. Atmos. Sci.*, **64**, 2076–2090, doi:10.1175/JAS3945.1.

Frierson, D. M. W., D. Kim, I.-S. Kang, M.-I. Lee, and J. Lin, 2010: Structure of AGCM-Simulated Convectively Coupled Kelvin Waves and Sensitivity to Convective Parameterization. *J. Atmos. Sci.*, **68**, 26–45, doi:10.1175/2010JAS3356.1.

Fuchs, Z., S. Gjorgjievska, and D. J. Raymond, 2012: Effects of Varying the Shape of the Convective Heating Profile on Convectively Coupled Gravity Waves and Moisture Modes. *J. Atmos. Sci.*, **69**, 2505–2519, doi:10.1175/JAS-D-11-0308.1.

Fuchs, Z. and D. J. Raymond, 2007: A simple, vertically resolved model of tropical disturbances with a humidity closure. *Tellus A*, **59**, 344–354, doi:10.1111/j.1600-0870.2007.00230.x.

Hannah, W. M. and E. D. Maloney, 2011: The role of moisture-convection feedbacks in simulating the maddenjulian oscillation. *J. Climate*, **24**, 2754–2770, doi:10.1175/2011JCLI3803.1.

Hannah, W. M. and E. D. Maloney, 2014: The moist static energy budget in NCAR CAM5 hindcasts during DYNAMO. *J. Adv. Model. Earth Syst.*, **6**, 420–440, doi:10.1002/2013MS000272.

Inoue, K. and L. E. Back, 2015: Column-integrated moist static energy budget analysis on various time scales during TOGA COARE. *J. Atmos. Sci.*, in press.

Johnson, R. H., P. E. Ciesielski, and K. A. Hart, 1996: Tropical inversions near the 0C level. *J. Atmos. Sci.*, **53**, 1838–1855, doi:10.1175/1520-0469(1996)053⟨1838:TINTL⟩2.0.CO;2.

Johnson, R. H., T. M. Rickenbach, S. A. Rutledge, P. E. Ciesielski, and W. H. Schubert, 1999: Trimodal characteristics of tropical convection. *J. Climate*, **12**, 2397–2418, doi:10.1175/1520-0442(1999)012⟨2397:TCOTC⟩2.0.CO;2.

Khouider, B. and A. J. Majda, 2006: A Simple Multicloud Parameterization for Convectively Coupled Tropical Waves. Part I: Linear Analysis. *J. Atmos. Sci.*, **63**, 1308–1323, doi:10.1175/JAS3677.1.

Kikuchi, K. and Y. N. Takayabu, 2004: The development of organized convection associated with the MJO during TOGA COARE IOP: Trimodal characteristics. *Geophys. Res. Lett.*, **31**, L10 101, doi:10.1029/2004GL019601.

Kiladis, G. N., M. C. Wheeler, P. T. Haertel, K. H. Straub, and P. E. Roundy, 2009: Convectively coupled equatorial waves. *Rev. Geophys.*, **47**, RG2003, doi:10.1029/2008RG000266.

Kim, D., et al., 2009: Application of MJO simulation diagnostics to climate models. *J. Climate*, **22**, 6413–6436, doi:10.1175/2009JCLI3063.1.

Kuang, Z., 2008a: Modeling the Interaction between Cumulus Convection and Linear Gravity Waves Using a Limited-Domain Cloud SystemResolving Model. *J. Atmos. Sci.*, **65**, 576–591, doi:10.1175/2007JAS2399.1.

Kuang, Z., 2008b: A moisture-stratiform instability for convectively coupled waves. *J. Atmos. Sci.*, **65**, 834–854, doi:10.1175/2007JAS2444.1.

Kuang, Z., 2009: Linear Response Functions of a Cumulus Ensemble to Temperature and Moisture Perturbations and Implications for the Dynamics of Convectively Coupled Waves. *J. Atmos. Sci.*, **67**, 941–962, doi:10.1175/2009JAS3260.1.

Kuang, Z., 2010: The wavelength dependence of the gross moist stability and the scale selection in the instability of column-integrated moist static energy. *J. Atmos. Sci.*, **68**, 61–74, doi:10.1175/2010JAS3591.1.

Lin, J.-L., et al., 2006: Tropical intraseasonal variability in 14 IPCC AR4 climate models. part i: Convective signals. *J. Climate*, **19 (12)**, 2665–2690, doi:10.1175/JCLI3735.1.

Maloney, E. D., 2009: The moist static energy budget of a composite tropical intraseasonal oscillation in a climate model. *J. Climate*, **22**, 711–729, doi:10.1175/2008JCLI2542.1.

Mapes, B. E., 2000: Convective inhibition, subgrid-scale triggering energy, and stratiform instability in a toy tropical wave model. *J. Atmos. Sci.*, **57**, 1515–1535, doi:10.1175/1520-0469(2000)057⟨1515:CISSTE⟩2.0.CO;2.

Masunaga, H. and T. S. L'Ecuyer, 2014: A mechanism of tropical convection inferred from observed variability in the moist static energy budget. *J. Atmos. Sci.*, **71**, 3747–3766, doi:10.1175/JAS-D-14-0015.1.

Neelin, J. D. and I. M. Held, 1987: Modeling tropical convergence based on the moist static energy budget. *Mon. Wea. Rev.*, **115**, 3–12, doi:10.1175/1520-0493(1987)115⟨0003:MTCBOT⟩2.0.CO;2.

Neelin, J. D. and J.-Y. Yu, 1994: Modes of Tropical Variability under Convective Adjustment and the MaddenJulian Oscillation. Part I: Analytical Theory. *J. Atmos. Sci.*, **51**, 1876–1894, doi:10.1175/1520-0469(1994)051⟨1876:MOTVUC⟩2.0.CO;2.

Neelin, J. D. and N. Zeng, 2000: A quasi-equilibrium tropical circulation model-formulation*. *J. Atmos. Sci.*, **57**, 1741–1766, doi:10.1175/1520-0469(2000)057⟨1741:AQETCM⟩2.0.CO;2.

Peters, M. E. and C. S. Bretherton, 2005: A Simplified Model of the Walker Circulation with an Interactive Ocean Mixed Layer and Cloud-Radiative Feedbacks. *J. Climate*, **18**, 4216–4234, doi:10.1175/JCLI3534.1.

Peters, M. E. and C. S. Bretherton, 2006: Structure of tropical variability from a vertical mode perspective. *Theor. Comput. Fluid Dyn.*, **20**, 501–524, doi:10.1007/s00162-006-0034-x.

Raymond, D. J. and Z. Fuchs, 2009: Moisture modes and the Madden-Julian oscillation. *J. Climate*, **22**, 3031–3046, doi:10.1175/2008JCLI2739.1.

Raymond, D. J., G. B. Raga, C. S. Bretherton, J. Molinari, C. Lpez-Carrillo, and . Fuchs, 2003: Convective Forcing in the Intertropical Convergence Zone of the Eastern Pacific. *J. Atmos. Sci.*, **60**, 2064–2082, doi:10.1175/1520-0469(2003)060⟨2064:CFITIC⟩2.0.CO;2.

Raymond, D. J., S. L. Sessions, and . Fuchs, 2007: A theory for the spinup of tropical depressions. *Q.J.R. Meteorol. Soc.*, **133**, 1743–1754, doi:10.1002/qj.125.

Raymond, D. J., S. L. Sessions, A. H. Sobel, and Z. Fuchs, 2009: The mechanics of gross moist stability. *J. Adv. Model. Earth Syst.*, **1**, 9, doi:10.3894/JAMES.2009.1.9.

Riley Dellaripa, E. M. and E. D. Maloney, 2015: Analysis of MJO wind-flux feedbacks in the Indian ocean using RAMA observations. *J. Meteor. Soc. Japan*, accepted.

Sobel, A. and E. Maloney, 2012: An idealized semi-empirical framework for modeling the Madden-Julian oscillation. *J. Atmos. Sci.*, **69**, 1691–1705, doi:10.1175/JAS-D-11-0118.1.

Sobel, A., S. Wang, and D. Kim, 2014: Moist static energy budget of the MJO during DYNAMO. *J. Atmos. Sci.*, **71**, 4276–4291, doi:10.1175/JAS-D-14-0052.1.

Sobel, A. H. and C. S. Bretherton, 2000: Modeling tropical precipitation in a single column. *J. Climate*, **13**, 4378–4392, doi:10.1175/1520-0442(2000)013⟨4378:MTPIAS⟩2.0.CO;2.

Sobel, A. H. and C. S. Bretherton, 2003: Large-scale waves interacting with deep convection in idealized mesoscale model simulations. *Tellus A*, **55**, 45–60, doi:10.1034/j.1600-0870.2003.201421.x.

Straub, K. H., P. T. Haertel, and G. N. Kiladis, 2010: An Analysis of Convectively Coupled Kelvin Waves in 20 WCRP CMIP3 Global Coupled Climate Models. *J. Climate*, **23**, 3031–3056, doi:10.1175/2009JCLI3422.1.

Straub, K. H. and G. N. Kiladis, 2003: The observed structure of convectively coupled Kelvin waves: Comparison with simple models of coupled wave instability. *J. Atmos. Sci.*, **60**, 1655–1668, doi:10.1175/1520-0469(2003)060⟨1655:TOSOCC⟩2.0.CO;2.

Sugiyama, M., 2009: The moisture mode in the quasi-equilibrium tropical circulation model. part I: Analysis based on the weak temperature gradient approximation. *J. Atmos. Sci.*, **66**, 1507–1523, doi:10.1175/2008JAS2690.1.

Tian, B. and V. Ramanathan, 2003: A Simple Moist Tropical Atmosphere Model: The Role of Cloud Radiative Forcing. *J. Climate*, **16**, 2086–2092, doi:10.1175/1520-0442(2003)016⟨2086:ASMTAM⟩2.0.CO;2.

Webster, P. J. and R. Lukas, 1992: TOGA COARE: The coupled ocean-atmosphere response experiment. *Bull. Amer. Meteor. Soc.*, **73 (9)**, 1377–1416, doi:10.1175/1520-0477(1992)073⟨1377:TCTCOR⟩2.0.CO;2.

Yanai, M., S. Esbensen, and J.-H. Chu, 1973: Determination of bulk properties of tropical cloud clusters from large-scale heat and moisture budgets. *J. Atmos. Sci.*, **30**, 611–627, doi:10.1175/1520-0469(1973)030⟨0611:DOBPOT⟩2.0.CO;2.

Yu, J., C. Chou, and J. D. Neelin, 1998: Estimating the gross moist stability of the tropical atmosphere*. *J. Atmos. Sci.*, **55**, 1354–1372, doi:10.1175/1520-0469(1998)055⟨1354:ETGMSO⟩2.0.CO;2.

Zebiak, S. E., 1986: Atmospheric Convergence Feedback in a Simple Model for El Nio. *Mon. Wea. Rev.*, **114**, 1263–1271, doi:10.1175/1520-0493(1986)114⟨1263:ACFIAS⟩2.0.CO;2.

Zhang, M. H. and J. L. Lin, 1997: Constrained variational analysis of sounding data based on column-integrated budgets of mass, heat, moisture, and momentum: Approach and application to ARM measurements. *J. Atmos. Sci.*, **54**, 1503–1524, doi:10.1175/1520-0469(1997)054⟨1503:CVAOSD⟩2.0.CO;2.

List of Figures

1 Schematic figures of a typical MSE profile and vertical velocity (omega) profiles in a bottom-heavy and a top-heavy shape. The leftward (rightward) arrows correspond to convergence (divergence). 41

2 (a): Power spectrum of $\partial\langle s\rangle/\partial t$. (b): Power spectrum of $\partial\langle q\rangle/\partial t$. (c): Time-series of raw (black), and daily running averaged $\partial\langle s\rangle/\partial t$ (blue) during TOGA COARE. (d): As in (c), but for $\partial\langle q\rangle/\partial t$. The specific humidity q is scaled by the latent heat of evaporation into the energy unit. 42

3 (a): Precipitation as a function of precipitable water $\langle q\rangle$. The black line was computed by a nonlinear least square fitting. 43

4 (a): Binned precipitation changes as a function of drying efficiency $\Gamma - \Gamma_C$, averaged in 12.5-percentile bins of $\Gamma - \Gamma_C$. The precipitation changes δP were computed by center differencing. (b): Binned probabilities of increase in precipitation as a function of $\Gamma - \Gamma_C$, averaged in the same bins as (a). The values subtracted from 100 % represent probabilities of decrease in precipitation. (c): Binned precipitation as a function of $\Gamma - \Gamma_C$, computed in the same way as above. For this figure, all data points with $\nabla \cdot \langle s\vec{v}\rangle$ less than 10 Wm^{-2} were remove to exclude convectively inactive times and to avoid division by zero. 44

5 Each component, horizontal GMS Γ_H (blue), vertical GMS Γ_V (black), and critical GMS Γ_C (red), decomposed from drying efficiency $\Gamma - \Gamma_C$ (gray), and averaged in the same bins as ones in Fig. 4. 45

6 (a): Vertical ω structures with respect to the values of vertical GMS Γ_V for convectively active times ($\nabla \cdot \langle s\vec{v} \rangle > 0$), averaged in 12.5-percentile bins of Γ_V. The star-marks on the x-axis denote the centers of the bins. (b): As in (a), but for convectively inactive times ($\nabla \cdot \langle s\vec{v} \rangle < 0$). The contour interval of (a) and (b) is 2*10^{-2} Pa/s. All points with $|\nabla \cdot \langle s\vec{v} \rangle|$ less than 10 Wm^{-2} are removed for avoiding division by zero. 46

7 As in Fig. 6a, but for temperature anomalies. The contour interval is 0.125 K. 47

8 (a): Scatter plot of column radiative heating $\langle Q_R \rangle$ as a function of vertically integrated total DSE export ($+\nabla \cdot \langle s\vec{v} \rangle$) for all data points including convectively inactive times. The solid line was computed by the linear least square fitting. The values in the upper left corner represent correlation coefficient (R) and mean square error (MSE) from the linear fit. (b)—(f): As in (a), but respectively for surface fluxes SF, $\langle Q_R \rangle + SF$, vertically integrated horizontal MSE export ($+\langle \vec{v} \cdot \nabla h \rangle$), vertically integrated vertical MSE export ($+\langle \omega \partial h / \partial p \rangle$), and the total MSE export ($+\nabla \cdot \langle h\vec{v} \rangle$). The dashed lines in (c) and (f) were computed by a regression through the origin. 48

9 (a): Binned vertical ω structures with respect to drying efficiency $\Gamma - \Gamma_C$ for convectively active times ($\nabla \cdot \langle s\vec{v} \rangle > 0$), averaged in the same bins as ones in Figs. 4 and 5. The star-marks on the x-axis denote the bin-centers. The contour interval is 2*10 $^{-2}$ Pa/s. (b): As in (a), but for temperature anomalies. The contour interval is 0.1 K 49

10 (a) and (b): As in Fig. 9, but for vertical and horizontal MSE advection, respectively. The contour interval is 5*10^{-3} J/kg/s. 50

11 Ratio of the variance of $\nabla \cdot \langle h\vec{v} \rangle$ to the variance of SF on different time-scales. The x-axis represents cut-off period of low-pass Lanczos filter with 151 weights, and the y-axis represents the ratio of var($\nabla \cdot \langle h\vec{v} \rangle$) to var($SF$). 51

12 (a), (b), and (c): As in Fig. 4, but as a function of GMS minus mean GMS, $\Gamma - \Gamma_0$. 52
13 Scatter plot of $\nabla \cdot \langle h\vec{v} \rangle$ vs. $\nabla \cdot \langle s\vec{v} \rangle$ with the GMS line as in Fig. 8f. The red/blue dots depict data points when the precipitation increases/decreases. 53

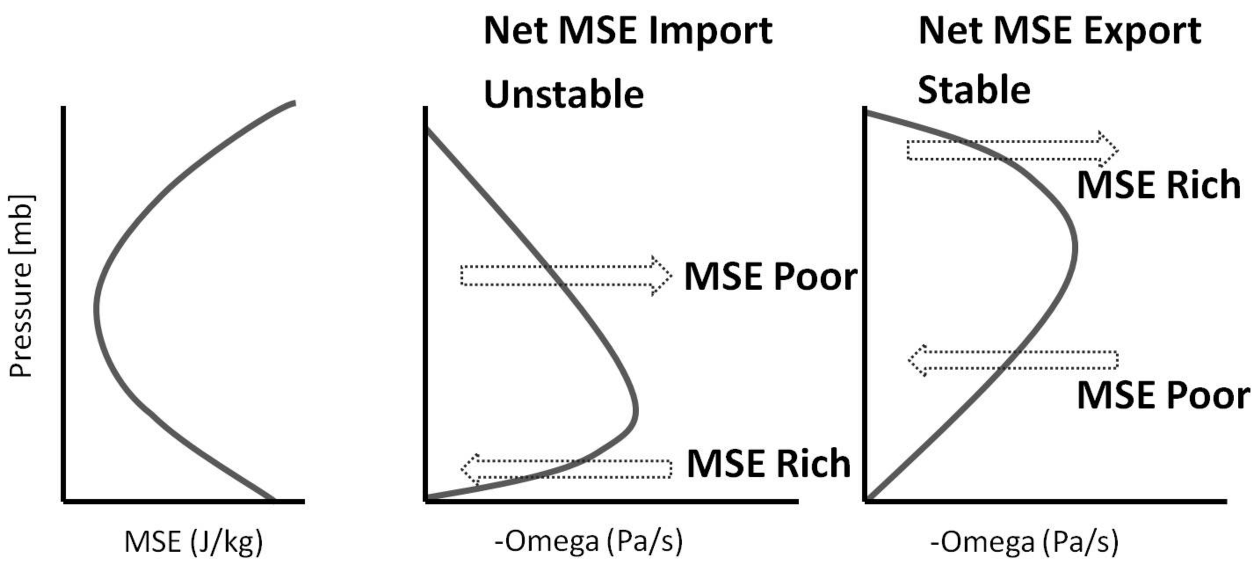

Fig. 1. Schematic figures of a typical MSE profile and vertical velocity (omega) profiles in a bottom-heavy and a top-heavy shape. The leftward (rightward) arrows correspond to convergence (divergence).

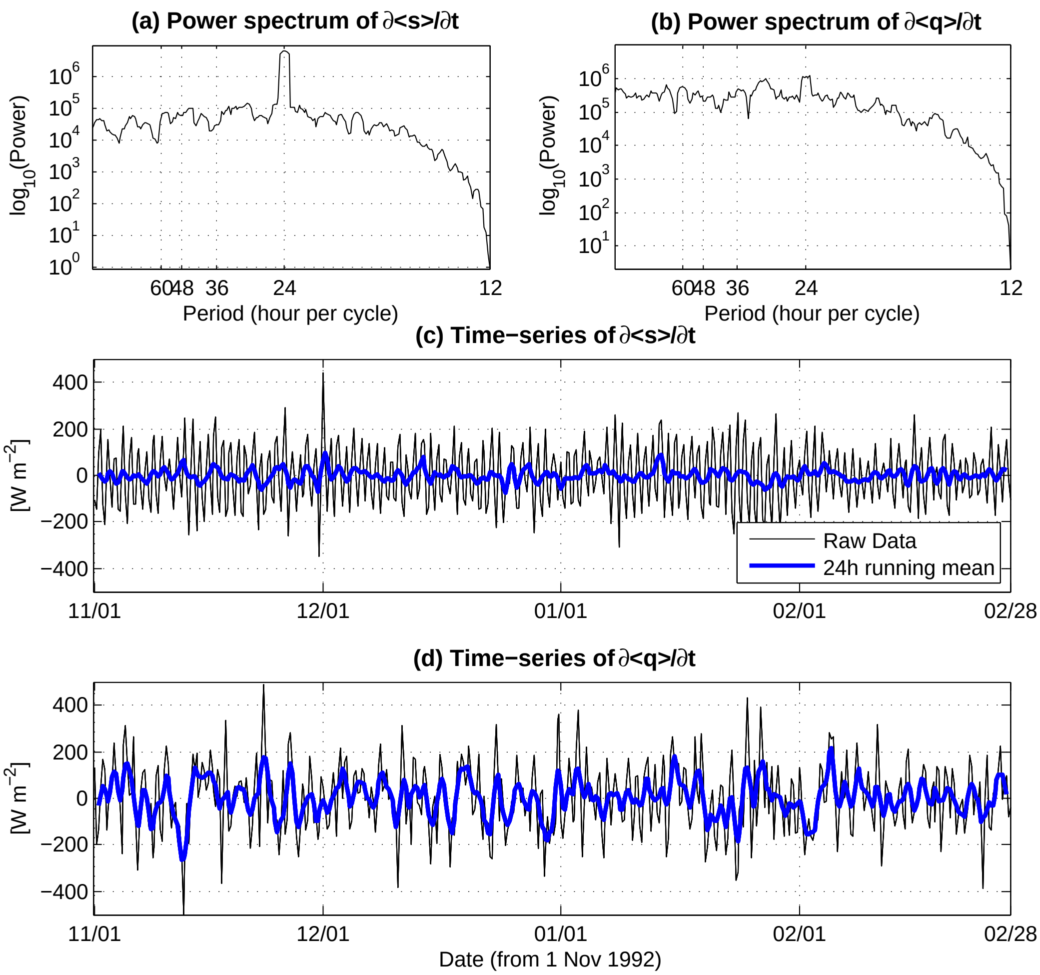

FIG. 2. (a): Power spectrum of $\partial\langle s\rangle/\partial t$. (b): Power spectrum of $\partial\langle q\rangle/\partial t$. (c): Time-series of raw (black), and daily running averaged $\partial\langle s\rangle/\partial t$ (blue) during TOGA COARE. (d): As in (c), but for $\partial\langle q\rangle/\partial t$. The specific humidity q is scaled by the latent heat of evaporation into the energy unit.

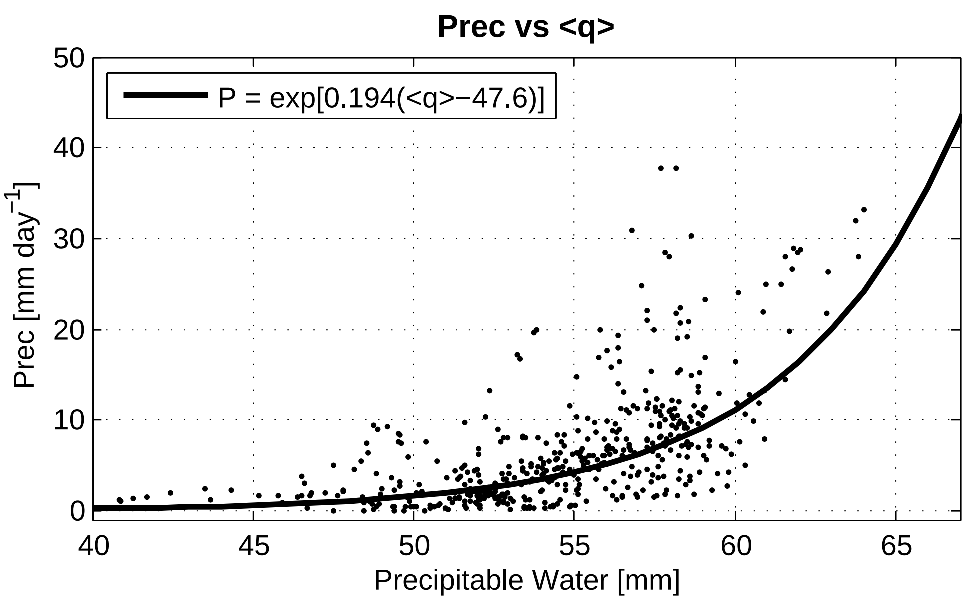

FIG. 3. (a): Precipitation as a function of precipitable water $\langle q \rangle$. The black line was computed by a nonlinear least square fitting.

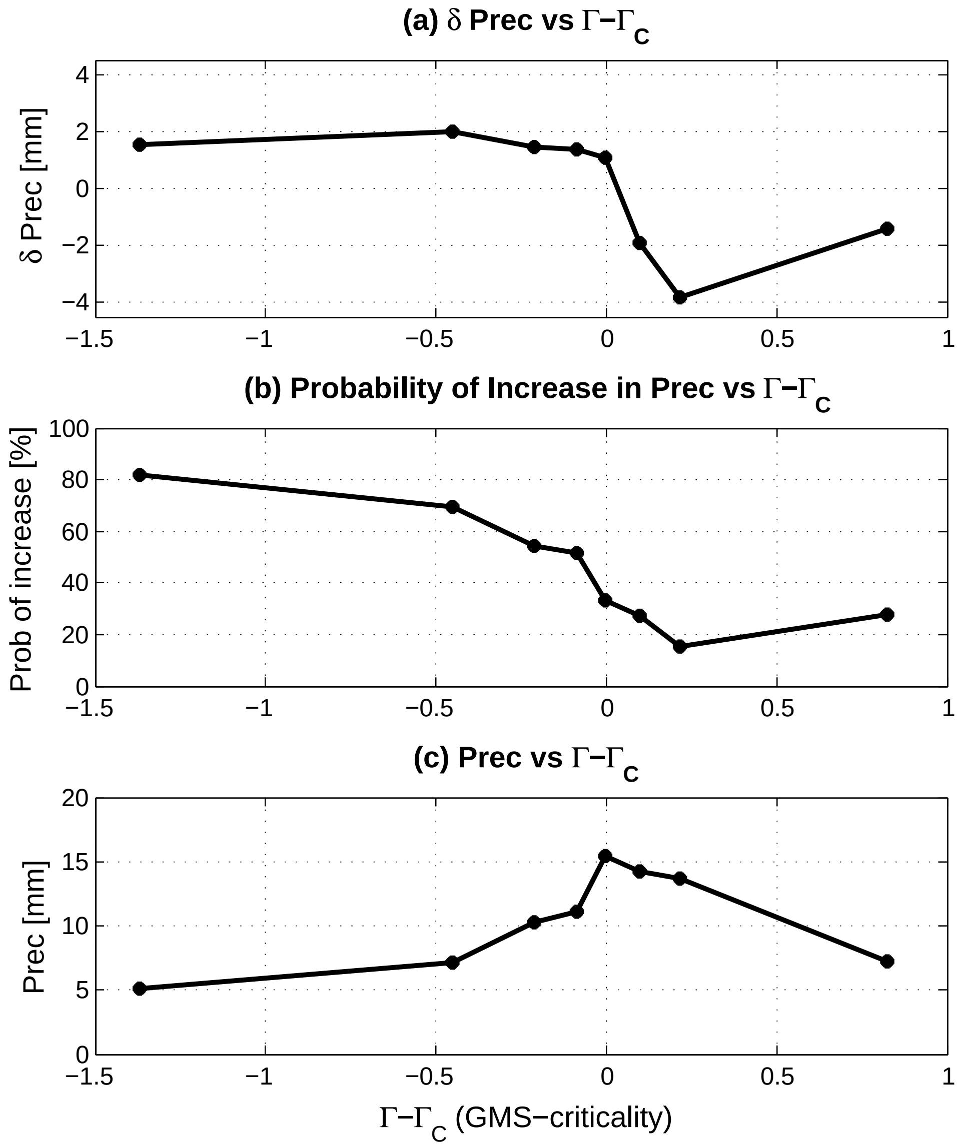

FIG. 4. (a): Binned precipitation changes as a function of drying efficiency $\Gamma - \Gamma_C$, averaged in 12.5-percentile bins of $\Gamma - \Gamma_C$. The precipitation changes δP were computed by center differencing. (b): Binned probabilities of increase in precipitation as a function of $\Gamma - \Gamma_C$, averaged in the same bins as (a). The values subtracted from 100 % represent probabilities of decrease in precipitation. (c): Binned precipitation as a function of $\Gamma - \Gamma_C$, computed in the same way as above. For this figure, all data points with $\nabla \cdot \langle s\vec{v} \rangle$ less than 10 Wm^{-2} were remove to exclude convectively inactive times and to avoid division by zero.

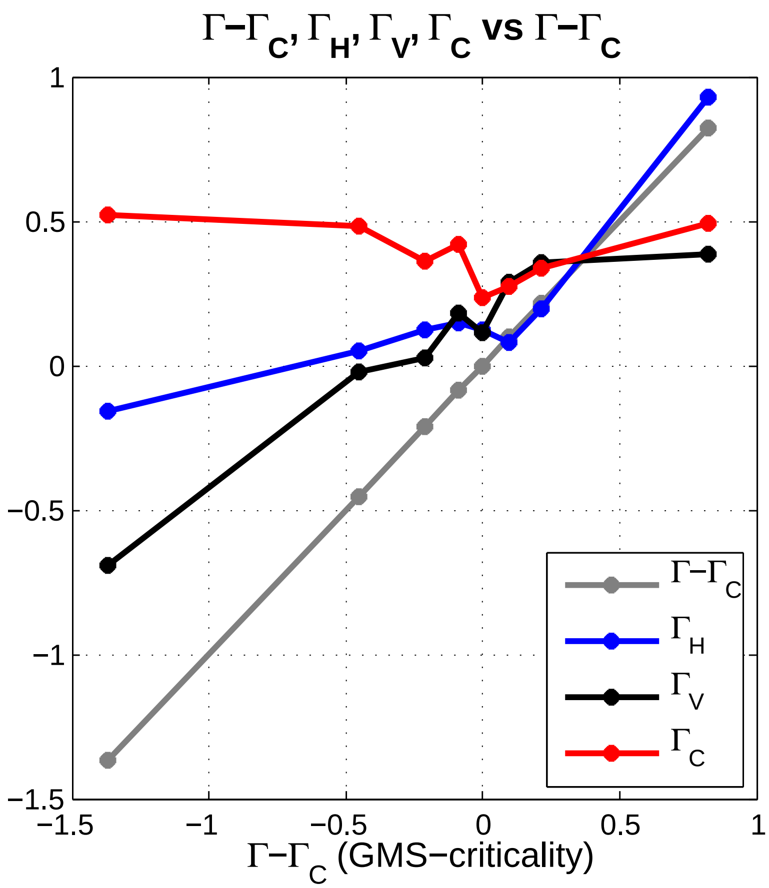

FIG. 5. Each component, horizontal GMS Γ_H (blue), vertical GMS Γ_V (black), and critical GMS Γ_C (red), decomposed from drying efficiency $\Gamma - \Gamma_C$ (gray), and averaged in the same bins as ones in Fig. 4.

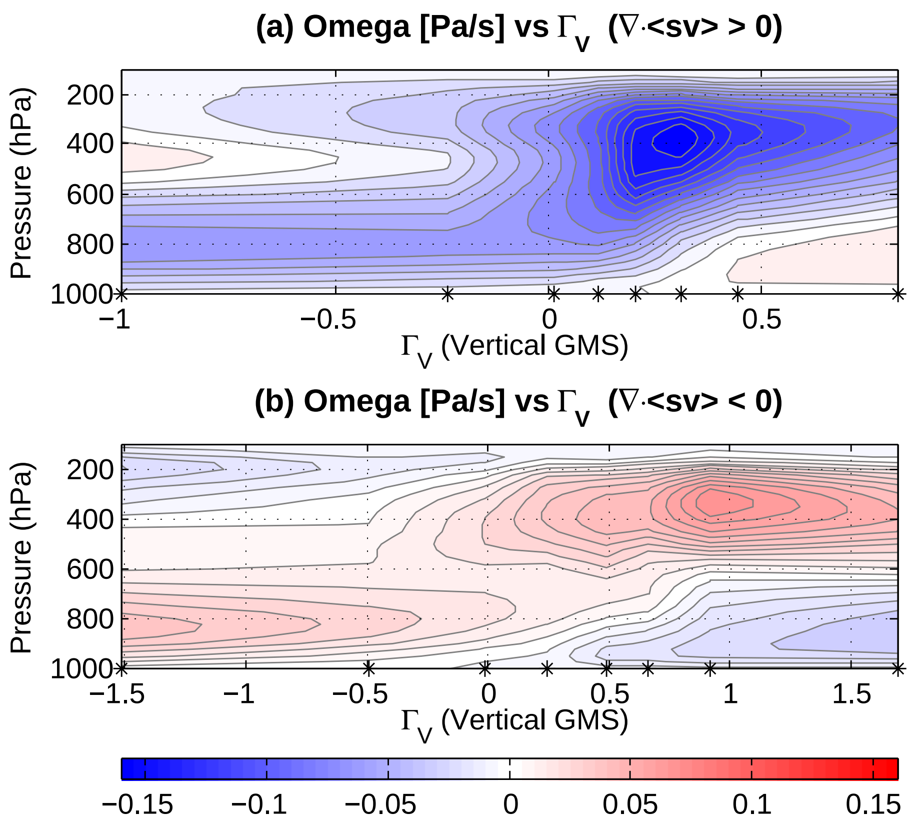

FIG. 6. (a): Vertical ω structures with respect to the values of vertical GMS Γ_V for convectively active times ($\nabla \cdot \langle s\vec{v} \rangle > 0$), averaged in 12.5-percentile bins of Γ_V. The star-marks on the x-axis denote the centers of the bins. (b): As in (a), but for convectively inactive times ($\nabla \cdot \langle s\vec{v} \rangle < 0$). The contour interval of (a) and (b) is $2*10^{-2}$ Pa/s. All points with $|\nabla \cdot \langle s\vec{v} \rangle|$ less than 10 Wm^{-2} are removed for avoiding division by zero.

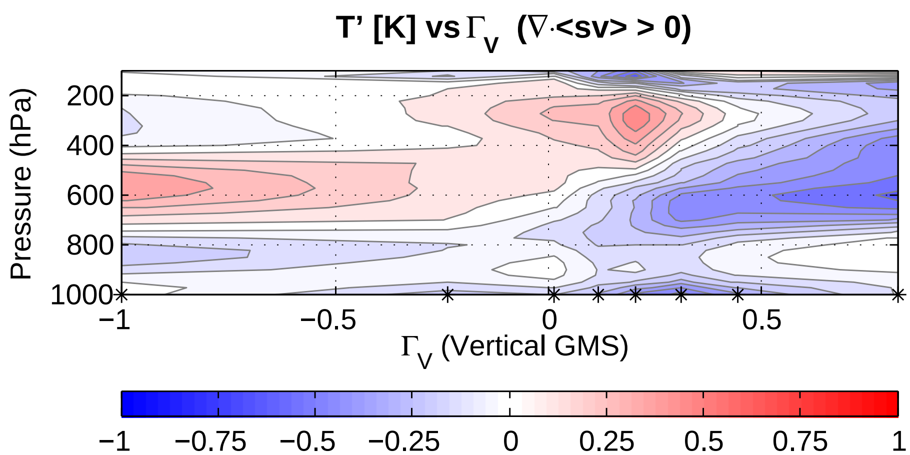

FIG. 7. As in Fig. 6a, but for temperature anomalies. The contour interval is 0.125 K.

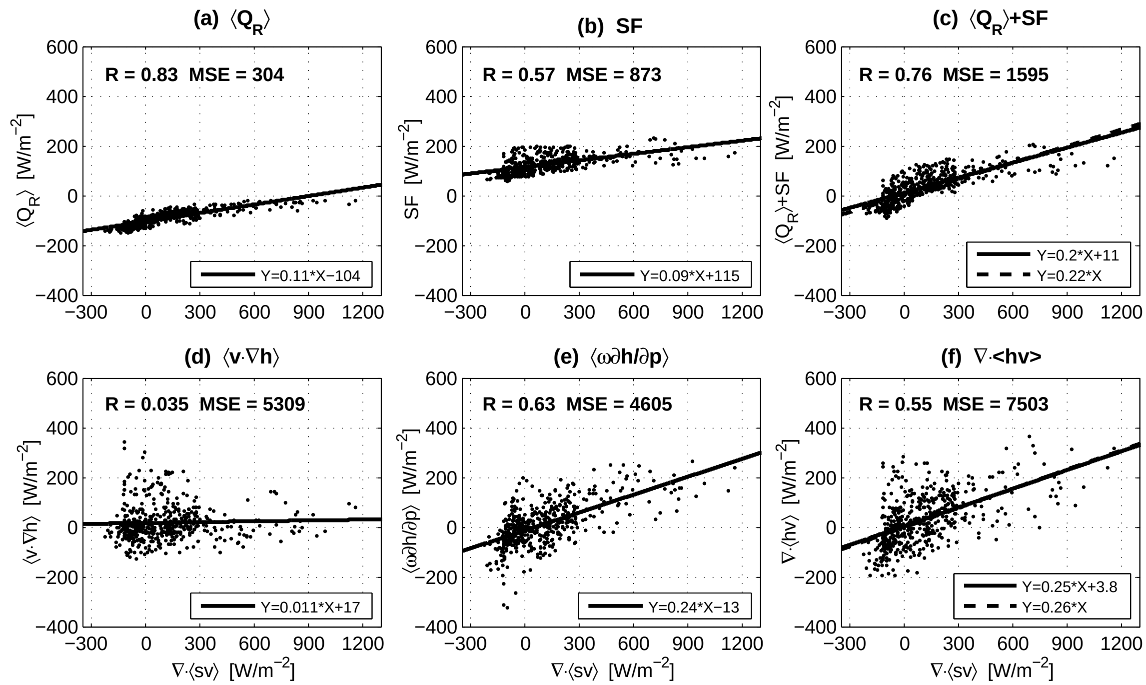

FIG. 8. (a): Scatter plot of column radiative heating $\langle Q_R \rangle$ as a function of vertically integrated total DSE export ($+\nabla \cdot \langle s\vec{v} \rangle$) for all data points including convectively inactive times. The solid line was computed by the linear least square fitting. The values in the upper left corner represent correlation coefficient (R) and mean square error (MSE) from the linear fit. (b)—(f): As in (a), but respectively for surface fluxes SF, $\langle Q_R \rangle + SF$, vertically integrated horizontal MSE export ($+\langle \vec{v} \cdot \nabla h \rangle$), vertically integrated vertical MSE export ($+\langle \omega \partial h/\partial p \rangle$), and the total MSE export ($+\nabla \cdot \langle h\vec{v} \rangle$). The dashed lines in (c) and (f) were computed by a regression through the origin.

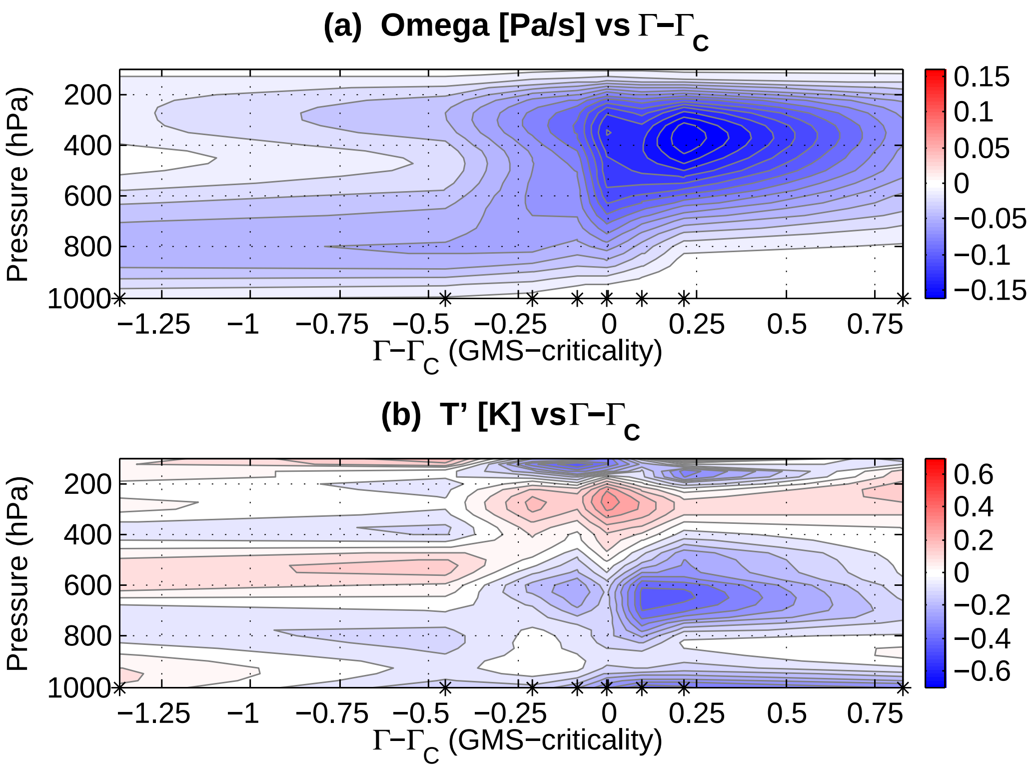

FIG. 9. (a): Binned vertical ω structures with respect to drying efficiency $\Gamma - \Gamma_C$ for convectively active times ($\nabla \cdot \langle s\vec{v} \rangle > 0$), averaged in the same bins as ones in Figs. 4 and 5. The star-marks on the x-axis denote the bin-centers. The contour interval is 2*10 $^{-2}$ Pa/s. (b): As in (a), but for temperature anomalies. The contour interval is 0.1 K

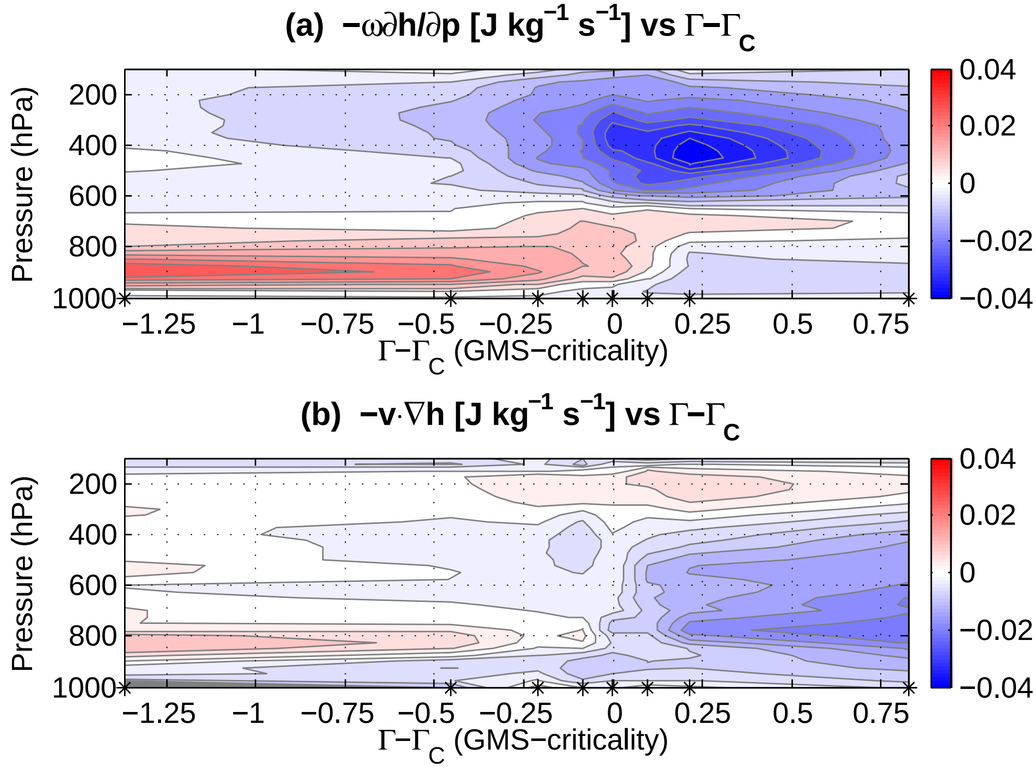

FIG. 10. (a) and (b): As in Fig. 9, but for vertical and horizontal MSE advection, respectively. The contour interval is $5*10^{-3}$ J/kg/s.

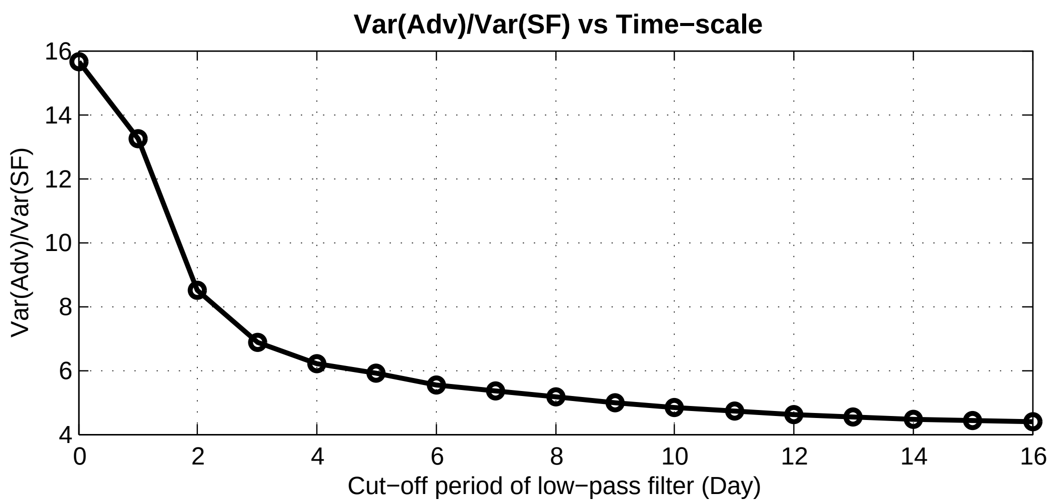

FIG. 11. Ratio of the variance of $\nabla \cdot \langle h\vec{v} \rangle$ to the variance of SF on different time-scales. The x-axis represents cut-off period of low-pass Lanczos filter with 151 weights, and the y-axis represents the ratio of $\mathrm{var}(\nabla \cdot \langle h\vec{v} \rangle)$ to $\mathrm{var}(SF)$.

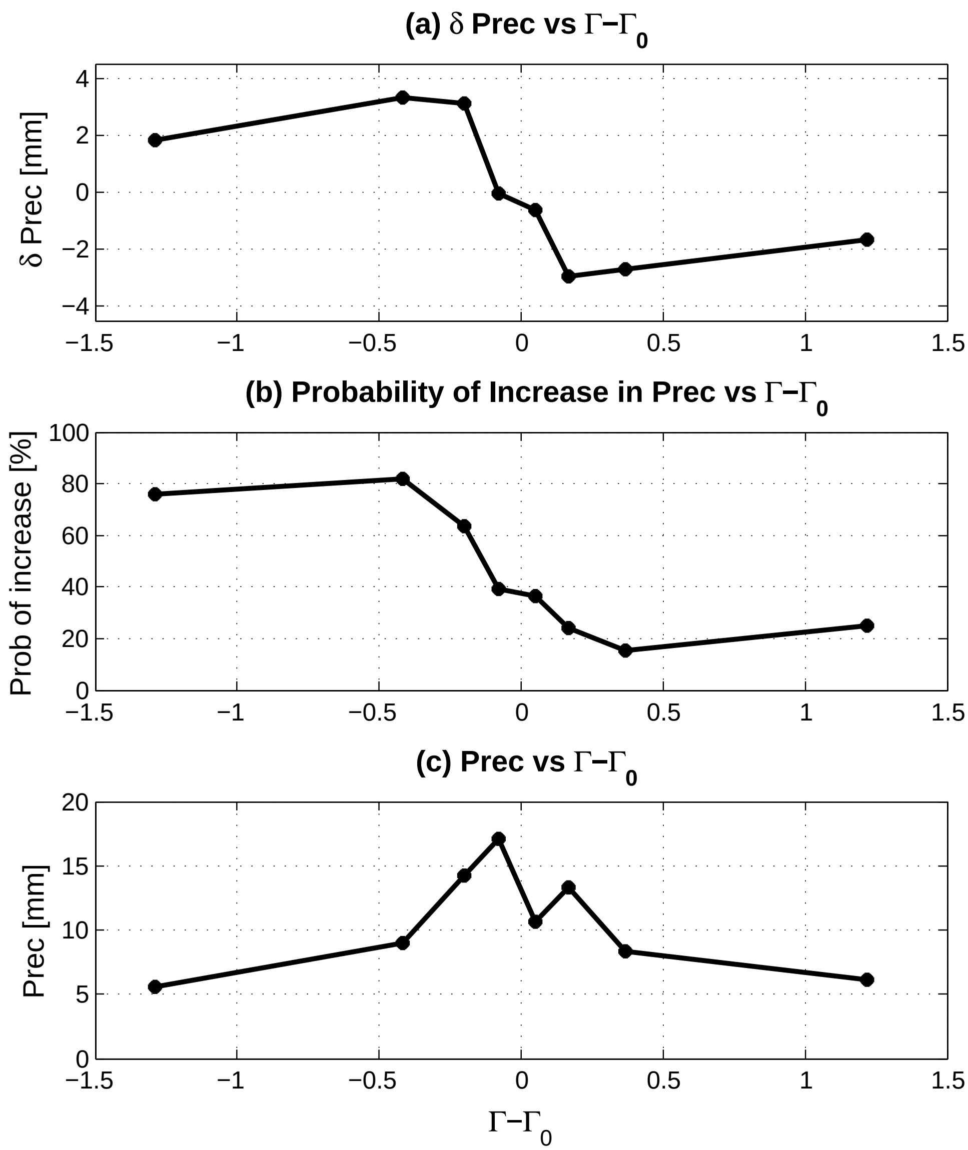

FIG. 12. (a), (b), and (c): As in Fig. 4, but as a function of GMS minus mean GMS, $\Gamma - \Gamma_0$.

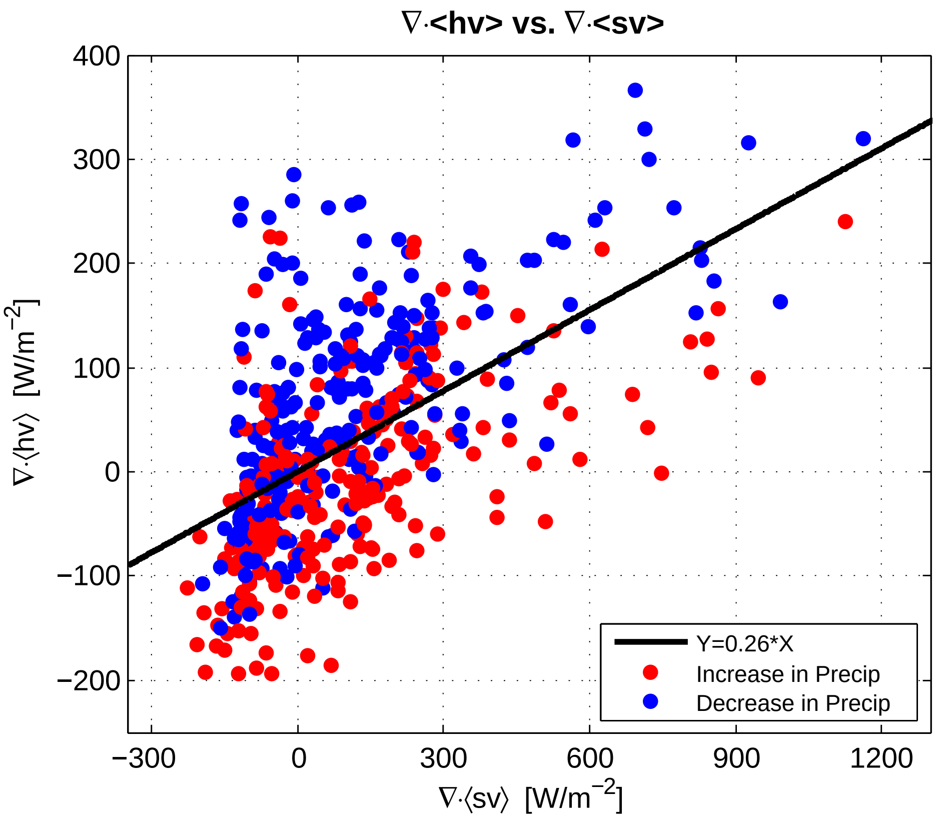

FIG. 13. Scatter plot of $\nabla \cdot \langle h\vec{v} \rangle$ vs. $\nabla \cdot \langle s\vec{v} \rangle$ with the GMS line as in Fig. 8f. The red/blue dots depict data points when the precipitation increases/decreases.